UC Santa Barbara

UC Santa Barbara Previously Published Works

Title

A versatile and modular quasi optics-based 200GHz dual dynamic nuclear polarization and electron paramagnetic resonance instrument

Permalink

https://escholarship.org/uc/item/3950r6r3

Authors

Siaw, Ting Ann
Leavesley, Alisa
Lund, Alicia
et al.

Publication Date

2016-03-01

DOI

10.1016/j.jmr.2015.12.012

Peer reviewed

A versatile and modular quasi optics-based 200 GHz dual dynamic nuclear polarization and electron paramagnetic resonance instrument

Ting Ann Siaw[1], **Alisa Leavesley**[1], **Alicia Lund**[1], **Ilia Kaminker**[1], and **Songi Han**[*,1]

[1]Department of Chemistry and Biochemistry, University of California Santa Barbara, Santa Barbara, CA 93106.

Abstract

Solid-state dynamic nuclear polarization (DNP) at higher magnetic fields (>3 T) and cryogenic temperatures (~2–90 K) has gained enormous interest and seen major technological advances as an NMR signal enhancing technique. Still, the current state of the art DNP operation is not at a state at which sample and freezing conditions can be rationally chosen and the DNP performance predicted *a priori*, but relies on purely empirical approaches. An important step towards rational optimization of DNP conditions is to have access to DNP instrumental capabilities to diagnose DNP performance and elucidate DNP mechanisms. The desired diagnoses include the measurement of the "DNP power curve", i.e. the microwave (MW) power dependence of DNP enhancement, the "DNP spectrum", i.e. the MW frequency dependence of DNP enhancement, the electron paramagnetic resonance (EPR) spectrum and the saturation and spectral diffusion properties of the EPR spectrum upon prolonged MW irradiation typical of continuous wave (CW) DNP, as well as various electron and nuclear spin relaxation parameters. Even basic measurements of these DNP parameters require versatile instrumentation at high magnetic fields not commercially available to date. In this article, we describe the detailed design of such a DNP instrument, powered by a solid-state MW source that is tunable between 193 – 201 GHz and outputs up to 140 mW of MW power. The quality and pathway of the transmitted and reflected MWs is controlled by a quasi-optics (QO) bridge and a corrugated waveguide, where the latter couples the MW from an open-space QO bridge to the sample located inside the superconducting magnet and *vice versa*. Crucially, the versatility of the solid-state MW source enables the automated acquisition of frequency swept DNP spectra, DNP power curves, the diagnosis of MW power and transmission, and frequency swept continuous wave (CW) and pulsed EPR experiments. The flexibility of the DNP instrument centered around the QO MW bridge will provide an efficient means to collect DNP data that is crucial for understanding the relationship between experimental and sample conditions, and the DNP performance. The modularity of this instrumental platform is suitable for future upgrades and extensions to include new experimental capabilities to meet contemporary DNP needs, including the simultaneous operation of two or

*Corresponding author: songi@chem.ucsb.edu.

more MW sources, time domain DNP, electron double resonance measurements, pulsed EPR operation, or simply the implementation of higher power MW amplifiers.

Keywords

solid state dynamic nuclear polarization; electron paramagnetic resonance; quasi optics; solid state MW source

1. Introduction

Solid state DNP (ssDNP) is an NMR signal-enhancing technique that is undergoing rapid development towards a surface, materials [1–12] and biosolids [13–25] characterization tool. The potential for ssDNP to transform NMR into a staple materials and biosolids characterization tool stems from the ability of this technique to generate an enhancement of NMR signal by $O(10^1\text{-}10^3)$ fold via polarization transfer from the electron spin of ssDNP-suitable radicals (also termed DNP agent) to the target nuclear spins. This signal gain, combined with a thermal polarization gain of $O(10^1\text{-}10^2)$ fold from cryogenic cooling to liquid nitrogen or helium temperatures and high magnetic fields, yields a total gain in nuclear spin polarization of $O(10^2\text{-}10^5)$ including the extreme ends. Considering that the reduction in the NMR experimental time corresponds to the square of this signal gain, ssDNP of frozen solids brings NMR into a new territory for materials and biosolids characterization capabilities by enabling studies of NMR-sensitive nuclei at concentrations and conditions that were conventionally inaccessible to NMR, given the infeasible or extremely long experimental times that may span several days to weeks of signal averaging. Wished-for study targets by ssDNP include the characterization of thin films, extended surfaces or low-γ nuclei in technologically important materials, electronic materials with cryogenic temperature-dependent properties, as well as conventionally weak signals reporting on structural or interfacial information in biological systems, including protein assembly, protein-RNA complexes, membrane proteins and cellular systems.

While there is immense potential for ssDNP to become a powerful characterization tool, much is still unknown about the principle operation of ssDNP, where the basic theoretical models for ssDNP even under static, and undoubtedly under magic angle spinning (MAS), conditions require further developments. In recent years, it has become apparent that the commonly accepted theoretical framework of thermal mixing (TM) [26–31] or explaining DNP under non-MAS and low temperatures (< 150 K) may not be consistent with experimental ssDNP observations, in particular the lineshapes of DNP spectra and the underlying saturation profile of the EPR spectrum. Consequently, several attempts were made to improve and expand beyond the TM formalism [32–37], notably by the Vega group [38–42], Tycko et al. [43–45], and Köckenberger et al. [46–48] who relied explicitly on the quantum mechanical, rather than thermodynamic, description of ssDNP. Two main ssDNP processes described by this framework are: (i) Solid effect (SE) DNP where MW irradiation of the forbidden transition of a single pair of electron and nucleus through the double quantum ($|\downarrow\downarrow\rangle$ to $|\uparrow\uparrow\rangle$) or zero quantum forbidden transitions ($|\downarrow\uparrow\rangle$ to $|\uparrow\downarrow\rangle$) results in the hyperpolarization of the nuclear spins and (ii) Cross effect (CE) DNP where MW irradiation

of the allowed electron spin transition of an electron-electron-nucleus (e-e-n) spin system transfers polarization from the coupled electron spins to the nuclear spins when the e-e frequency difference matches that of the nuclear Larmor frequency. The two dipolar coupled electron spins responsible for flipping a nuclear spin may not be the electron spins that are directly excited by microwave (MW) irradiation, nor the ones chemically tethered as part of one biradical molecule, where the e-e flip-flop transitions can also be activated by spectral diffusion, giving rise to the term indirect CE (iCE) [49] or multi-electron spin CE [50]. This does not change the fact that an allowed EPR transition occurs to initiate a flip-flop transition of a dipolar coupled electron spin pair that is ultimately responsible for a nuclear spin flip. Clearly, electron spin spectral diffusion is an important factor for distributing electron spin polarization that must be taken into account when quantifying DNP performance. While the debuted quantum mechanical models improved the ability to fit the ssDNP spectra lineshapes [51–53], they do not fully describe or easily predict the outcome of ssDNP experiments, such as the shape of the ssDNP spectrum, mainly because critical experimental parameters are usually unknown, and thus are estimated when modeling DNP data. These include electron T_1 and T_2 relaxation time at the same field and temperatures of the DNP operation, electron spectral diffusion rate, EPR saturation profile, as well as nuclear spin diffusion properties under operational DNP conditions. The need to further develop the understanding of ssDNP mechanisms and to generate practically useful theoretical models is illuminated by highly interesting observations reported on in the literature that are contrary to conventional wisdom, while theoretical explanations were only provided for some observations about how certain experimental parameters may affect the ssDNP properties (this is by no means a comprehensive list of all ssDNP effects):

1.   Electron double resonance (ELDOR) studies [49,54] reveal that below 40 K at 3.34 T, the saturated area of the EPR spectrum of nitroxide radicals at tens of mM concentration— commonly for ssDNP operation—with monochromatic MW irradiation is rather significant, indicating that electron spectral diffusion is highly efficient under those experimental conditions.

2.   Applying MW frequency/field modulation increases the ssDNP enhancement by almost an order of magnitude, especially at low nitroxide concentrations [55,56], by virtue of increasing the frequency excitation bandwidth over the monochromatic MW source.

3.   DNP operation below 6 K and at 7 T led to the observation of an oversaturation regime, where DNP enhancement no longer increases, but decreases with increasing MW power beyond a threshold value. This is only observed with samples containing high radical concentrations, e.g. 40 mM nitroxide radical in frozen solution, with transmitted MW powers of order 50–70 mW and at temperatures below 6 K [50]. This can be reconciled with a broad saturation of the nitroxide EPR spectrum due to an exceedingly large excitation bandwidth that diminishes the electron spin polarization differential beyond a saturation threshold, which is consistent with observations of (1) and (2). Corroborating new data will be presented in this article.

4. More rigid radical architectures of biradicals or oligoradicals can provide higher ssDNP enhancement values, the merit of which turns out particularly critical at higher magnetic fields [15,57–61].

5. Adding dielectric particles that scatter microwaves into or at the ends of MAS rotors can help distribute the MW field, increasing ssDNP enhancement by a factor of 2 [19,62].

6. MAS operation in the presence of ssDNP-active radicals, but in the absence of MW irradiation, can result in depolarization of the nuclear spins, leading to NMR signal loss, indicating that the overall nuclear polarization is effectively lower [44,45,63–65]. The depolarization effect seems particularly strong with the types of radicals yielding high DNP enhancements, implying that some of the enhancement effect is due to the decrease in the unenhanced reference signal amplitude.

7. Observation of an optimum MAS spinning speed that yields the highest ssDNP enhancement, where the optimum depends on temperature and other factors [45,60,63,64,66].

These example observations reveal that there are unexplored ssDNP parameters that affect the ssDNP enhancement, which prevents *a priori* prediction of ssDNP performance for a given set of experimental and sample conditions. Therefore, currently, the only viable method to optimize ssDNP condition is through empirical determination of operating conditions.

The need to better understand ssDNP processes, coupled with the need to explore a wide DNP parameter space for performance optimization calls for a versatile ssDNP hardware. The required hardware performance is reflected in the type of experiments that yielded the observations listed above—MW frequency/field modulation, MW power stepping, EPR detection (particularly ELDOR), MW frequency sweeps, EPR relaxation measurements, etc. The combination of these hardware capabilities are not offered with any commercial ssDNP instrument platform. Instead, select capabilities are available through different ssDNP setups, as listed below. As a side note, even though dissolution DNP targets solution NMR application, the DNP process occurs in the solid-state, which is why it is listed under ssDNP systems, while important developments on Overhauser DNP at low and high magnetic fields are not included in this article.

1. **Gyrotron-powered MAS DNP systems**: High resolution MAS-gyroton systems operating at > 5 T and 90–150 K, developed by Griffin et al. and commercialized by Bruker Biospin. Gyrotron systems offer high microwave power output between 5–35 W, allowing for DNP operation at higher temperatures of 90–150 K [67–75], while recent developments by Idehara et al. and Gaël de Paëpe et al. also enable liquid helium operation around 30 K with gyrotron-powered DNP systems [76,77]. Notably, the Matsuki, Idehara and Fujiwara et al. [78] system relies on a dual gytrotron source at 460 GHz and 459–461 GHz for MAS DNP operation at 16.4 T and liquid helium temperatures. Additionally, Pike et. al. [19] have developed a system that uses the fundamental (187 GHz) and second harmonic (395 GHz) of a gyrotron source for DNP signal detection at 6.7 and 14 T. A recent theoretical

calculation of pulsed gyrotron operation has also been performed by Barnes et al., which provides an outlook for EPR operation of a high powered gyrotron source [79]. In general, a gyrotron source can offer a frequency bandwidth of up to 3 GHz, but the MW power is not constant over this frequency range. This means that DNP spectra can only be acquired reliably using a field sweep, instead of a frequency sweep. At the moment, EPR detection is not feasible with these systems due to amplitude fluctuations of the gyrotron source output. The gyrotron system has been successfully applied for enhanced ssNMR studies of biological systems [13,16,17,19–25] and materials surfaces [12,80,81]. Significant progress in DNP-enhanced MAS NMR can be attributed to the design and development of novel DNP polarizing agent design, such as TOTAPOL, AMUPOL, bTbk, etc. with superior performance to mono-nitroxide radicals under typical MAS DNP operating conditions at approximately 90 K [57–60].

2. **Dissolution DNP systems**: Dissolution DNP systems operating at 1.2 K and 3.35 T were initially developed by Larsen and co-workers [82]. These systems traditionally polarize frozen samples at ~ 1.2 K and 3.35 T to achieve high nuclear spin polarization, followed by rapid melting of the sample for injection into MRI subjects or samples for spectroscopy or imaging of enzymatic or other chemical processes by DNP-enhanced NMR detection at higher magnetic fields [83–87]. There have been commercial systems developed by general electric (GE) healthcare / Oxford Instruments, most recently upgraded to operate at a higher magnetic field of 5 T in a system known as SpinLab, while modified or home-built dissolution DNP systems operating at 3.35 T or 6.7 T have also been presented [56]. Interestingly, using a dissolution DNP polarizer system, Jannin et al. have recently demonstrated an order of magnitude improvement in DNP enhancement for a 10 mM nitroxide solution when frequency modulation is applied at 1.2 K and 6.7 T [56].

3. **Nottingham Köckenberger lab ssDNP/EPR systems**: One of the Köckenberger dissolution DNP systems was built around a two-center magnet for polarization at 3.35 T and NMR detection at 9.4 T with a non-zero field transition between the two and included a QO bridge for CW EPR detection at 94 GHz. This system was designed to minimize polarization loss when transferring the sample from the polarizing field (3.35 T) to the detection field (9.4 T) [83]. Another unique spectrometer in the Köckenberger lab is a 3.35 T dissolution DNP spectrometer with longitudinal EPR detection capabilities [88]. This spectrometer employs a 200 mW diode source with a sweepable range of 650 MHz, which allows for the acquisition of frequency or amplitude modulated CW EPR spectra as well as ELDOR experiments. The Köckenberger group was the first group to measure the TEMPO ELDOR spectrum under DNP conditions for the purpose of directly measuring the extent to which the EPR line of TEMPO is affected upon prolonged microwave irradiation [88].

4. **Massachusetts Institute of Technology (MIT) Griffin lab ssDNP/EPR system**: A dual pulsed-EPR/DNP spectrometer operating at 5 T (140 GHz electron / 212 MHz 1H) is described by Smith et. al. [89] This instrument was designed to

perform pulsed EPR and DNP at temperatures of less than 100 K under static (non-MAS) conditions. This system was built in order to study the mechanism of the DNP process, where knowledge of the spin relaxation times of the electron spins in the sample are important for understanding the DNP enhancement process. This spectrometer also has the capability to perform ELDOR and electron nuclear double resonance (ENDOR) experiments. With these capabilities one can directly measure the saturation profile of an EPR spectrum upon MW irradiation of the sample under DNP conditions.

5. **Weizmann Institute Vega and Goldfarb lab ssDNP/EPR system**: A dual EPR/DNP spectrometer operating at 3.34 T (95GHz electron / 144MHz 1H) was built at the Weizmann Institute of Science by the joint effort of the groups of Goldfarb and Vega. This instrument was designed to concurrently perform EPR and DNP experiments at low temperature (< 100 K) under static (non-MAS) conditions and at 3.34 T [90]. The EPR MW bridge of this DNP system was constructed based on a design previously refined by the Goldfarb group [91]. The Vega and Goldfarb groups have contributed significantly to the quantum mechanical understanding [38– 42,49,54] of DNP processes through ELDOR [49] and DNP data [51–53] acquired using this spectrometer.

6. **NIH Tycko lab ssDNP system**: A MAS-DNP system operating at 9.4 T and down to 25 K temperatures, initially utilizing a low powered diode MW source [61], and recently upgraded with a higher powered extended interaction oscillator (EIO) MW source [61], was developed by Tycko, Thurber, and co-workers at the National Institute of Health (NIH). This MAS system can operate at liquid helium temperatures down to 25 K by using a novel MAS design that employs an elongated MAS rotor where the ends of the rotor are spun with cold nitrogen gas and the center of the rotor cooled with liquid helium [92]. Tycko and co-workers have been performing ssDNP-enhanced NMR studies of frozen samples of peptides [15,61] and protein fibrils of amyloid beta [14]. Tycko and co-workers have also contributed to the design of oligoradicals [15,61], and the understanding of MAS-DNP effects [44,45].

7. **UCSB Han lab ssDNP/EPR system**: A dual EPR/DNP spectrometer operating at 7 T and liquid helium temperatures, powered by a tunable solid-state diode source (193–201 GHz), as developed by Han and co-workers at the University of California, Santa Barbara (UCSB) [93]. A quasi optical (QO) MW bridge is used to manipulate the quality, amplitude, frequency and shape of the transmitted and reflected microwaves (e.g. for EPR detection). The QO DNP setup operates at room temperature down to 4 K on static samples, and at room temperature down to 25 K under MAS operation. Han et al. have observed the effect of oversaturation for a 40 mM nitroxide glass solution at 4 K [50], and also recently demonstrated targeted adsorption of DNP polarizing agents for characterizing catalyst active sites [3].

From the summary of ssDNP systems provided above and summarized in Table 1, it can be seen that the hardware capabilities vary significantly between the different ssDNP systems

currently available. Most ssDNP systems are focused on particular application targets, while the hardware improvements pursued are often centered on the saturation performance by MW irradiation, notably by higher power output or frequency modulation. However, systematic ssDNP studies focused on the spin physics of the electron-nuclear polarization transfer mechanism and quantification of DNP enhancement require additional hardware capabilities, such as ssDNP frequency sweeps, CW and pulsed EPR experiments and ELDOR measurements—such capabilities are currently available at 3.34 T [88,90], and some at 5 T [89]. The UCSB ssDNP system of the Han lab operating at 7 T is complementary to existing hardware, and consists of a modular DNP hardware platform that allows for static and MAS NMR operation, and is designed to perform EPR and ELDOR experiments. The versatility of the UCSB Han lab's ssDNP system arises from relying on a QO MW bridge. In fact, the use of QO is a common mode of operation for high field EPR setups [94–100], as first demonstrated by Freed and co-workers [96], and provides the means for low loss transmission of MWs, which is critical when employing low power solid-state diode sources to drive DNP or EPR experiments. Furthermore, QO is the only approach in the sub-Terahertz MW frequency regime to efficiently combine, isolate and re-direct MWs for EPR detection and experiments. Hence, a QO MW bridge is an extremely versatile tool that enables dual DNP/EPR operation, as will be described in detail in this perspectives article. The same QO bridge is compatible with alternative MW sources to a solid-state diode source, e.g. Klystron oscillators or high-power gyrotron sources. The NIH ssDNP setup by Tycko and coworkers that was originally powered by a diode source (Virginia Diodes Inc.) has already been modified to be powered by a klystron oscillator (Communications & Power Industries LLC) that can output around 0.8 W of MW power [15]. However, for the most versatile DNP and EPR operation, the use of a solid-state source, despite its lower power MW output, is necessary to enable broadband (10 GHz frequency sweep width) MW tuning, precise MW amplitude and frequency control (10 Hz or better resolution), and the ability to apply amplitude (including pulsing ability and shaped waveforms) and frequency modulation of the transmitted microwaves. The UCSB system is built to maximize the versatile operation to enable the measurement of a wide range of DNP parameters and DNP mechanism-relevant EPR parameters. The modularity of the system provided by the QO-based MW bridge allows for component-by-component upgrades when better capabilities are available in the future, e.g. a currently difficult to get high-power MW amplifier, without the need to purchase an entirely new DNP system. If this mode of operation is commercialized, it will enable full customization of DNP systems according to cost and experimental needs. We believe that this will be highly beneficial tool for the magnetic resonance community.

In this article, we will describe the construction of the UCSB DNP system by building upon an existing 7 T Bruker superconducting magnet and spectrometer system. The focus here will be the establishment of a basic hardware framework for performing 4–290 K NMR, DNP and EPR experiments, MW and DNP performance diagnostics, and automation of DNP data acquisition. This was enabled by the implementation of the QO MW bridge design and centralized instrument control using the Specman4EPR software (Boris Epel, Femi Instruments, LLC) [101], both of which can be further expanded or modified to achieve wished-for experimental goals. Using these capabilities, we demonstrate the ability

to evaluate and diagnose the MW performance, specifically the MW power stability across time and frequency, Gaussian beam profile, MW insertion losses across MW transmission hardware, as well as to establish precise amplitude and frequency control of the MW. The precise MW amplitude and frequency control enables automated acquisition of frequency swept DNP spectra (enhancement vs. MW frequency) and power curves (enhancement vs. MW power), both of which are important for understanding DNP processes, and last but not least, frequency stepped pulsed and CW EPR measurements. We will describe the QO bridge design for pulsed EPR ELDOR implementations and superheterodyne detection of pulsed and CW EPR spectra using frequency stepped, field-modulated, detection in lieu of the conventional field swept (and field-modulated) EPR detection approach, by presenting proof-of-principle data of standard Mn^{2+} and diamond samples acquired at room temperature. The work presented in this article intends to establish a basic framework for dual DNP-EPR operation at 7 T and beyond, with the necessary configurations for implementing future hardware upgrades to expand the DNP-EPR toolkit.

2. Instrument Overview

The UCSB 200 GHz dual DNP/EPR spectrometer is a highly modular system centered around the flexibility of the QO-based MW bridge. The current prototype DNP system discussed in this article is a result of hardware additions and modifications to an existing magnet and spectrometer system [93,102], specifically a 300 MHz, 89 mm wide bore Bruker superconducting magnet and a Bruker Avance D300WB console with a 1 kW rf amplifier. Crucially, this system can be constructed from the ground up onto *any* existing high-field magnet and NMR spectrometer console, provided that solid-state MW sources are available at the adequate MW frequency (currently, sufficiently high-power diode sources are available for 7–9 Tesla fields by VDI Inc.) with (but not limited to) the following additions (a sketch of the overall setup is shown in Fig. 1), the details of which will be described:

1. Cryostat (or thermostat) for temperature control

2. DNP probe insert consisting of a waveguide, NMR coil, and EPR modulation coil

3. MW support structure

4. MW bridge consisting of MW source and quasi-optical components

5. EPR detection hardware

6. Centralized control software

2.1. Cryostat

Cryogenic cooling of the sample to liquid helium temperatures <50 K can yield high nuclear spin polarization (P_n) from DNP operation when irradiating with a solid-state MW source. We recently reported as high as P_n = 61% [50,102,103], which is in part due to high initial P_e (83% at 4 K and 7.049 T), long T_{1e} of (10^1-10^2) ms found for nitroxide radicals at 4 K temperatures, and high spectral diffusion rate for nitroxide radicals found at high radical concentrations on the order of 20 mM [49,50,60]. In order to operate at temperatures between 4–290 K, we employ a custom STVP-200-NMR continuous flow cryostat (Janis Research Co. LLC). A Sogevac SV65B rotary vane pump (Oerlikon Leybold Vacuum) is

connected to the outlet of the cryostat to evacuate the sample chamber, while liquid helium is flowed into the inlet from a liquid helium dewar (PraxAir) using a continuous-flow liquid helium transfer line with flow control (Janis Research Co. LLC). Precise temperature control is maintained by the heating of the incoming liquid helium with a voltage controlled resistive heater, while the temperature is simultaneously measured with a Cernox temperature sensor (Lakeshore Cryogenics). The Cernox temperature measurement and heater voltage are controlled by a LabView program where a proportional-integral-derivative (PID) algorithm controls the heater voltage output from a 0–35 V, 15 A power supply to maintain a temperature stability minimum of +/− 0.02 K. The cryostat is top-loaded into the bore of the magnet, and the cryostat has a hollow bore surrounded by a vacuum jacket where the DNP probe is top-loaded into and secured with a KF-50 clamp to create a vacuum seal. Refining the choice of components to achieve greater vacuum sealing will enable even lower temperature operation down to approximately 2 K using basically the same setup.

2.2. Probe insert

The probe insert, shown in Fig. 2a, is a support structure that houses the MW waveguide, the NMR probe and mechanical actuators for tuning and matching the NMR circuit. This entire probe insert is top-loaded into the cryostat bore, so that the final position of the NMR coil and sample is at the sweet spot of the magnet, with only a small section of the waveguide protruding out of the cryostat to capture the incoming MW beam from the MW bridge through a transparent Polymethylpentene (TPX®) aperture. The corrugated MW waveguide (Thomas Keating, LTD) is held in the center of the probe insert and consists of a hollow cylinder made of german silver that is smooth on the outside but corrugated on the inside, where the MWs guided to the sample are in contact with these corrugations. The corrugations of the waveguide ensure minimal MW power loss (~0.5 dB) of the HE_{11} MW mode. Alternatively, a low cost smooth walled waveguide can be employed, which supports TEM modes (comparatively, corrugated waveguides support hybrid modes, i.e. HE modes). In order to utilize this low cost option, it is important to compare the coupling from free space (TEM_{00} mode) to a smooth walled or corrugated waveguide, and the shortcomings of using a smooth walled waveguide. For a corrugated waveguide, the optimal coupling between the Gaussian TEM_{00} mode and the HE_{11} mode of the waveguide requires a MW beam radius that is 0.64 times that of the waveguide radius [104]. This will result in 98% coupling, where the 2 % power difference is mainly converted to higher order modes [105,106]. A smooth walled waveguide supporting a TE_{11} mode requires the MW beam radius to be 0.76 times the waveguide radius in order to have 91 % coupling efficiency in an idealized case [104], with 9 % power loss mainly converted into higher order modes [106]. A complete analysis of mode matching between the MW beam and the waveguide requires a full modal decomposition of the fields for each type of waveguide, where the MW beams can generally be represented as Bessel-like profiles [107]. In addition to MW and waveguide mode mismatch, smooth walled waveguides can have significant attenuation due to resistive wall losses (0.74% for a 0.9 m waveguide) compared to corrugated waveguides (negligible) [106]. Thus, in order to minimize coupling losses between the MW beam and the waveguide, a smooth walled waveguide should have a radius that is 0.842 times smaller than a corrugated waveguide. The inner diameter (ID) of our corrugated MW waveguide is 12.5

mm for most of the length (not including corrugations), but tapers to 5.3 mm to concentrate the MW beam to a smaller waist compatible with the sample size along the last 70 mm of the waveguide. After this waveguide taper, another short (43 mm) waveguide extension (Fig. 2b and c) guides the 5.3 mm waist MW beam to the sample and NMR probe located at the sweet spot of the magnet. In Section 3.2.2, we will analyze the performance of four different waveguide extensions constructed from copper, zirconia, and a thin layer of gold with two types of plastic supports (Fig. 2c).

The NMR or EPR probe module and sample are placed at the end of the waveguide extension. The NMR probe module consists of an Alderman-Grant ^{1}H coil inductively coupled to a pickup loop for transmission and detection (Fig. 2d), which is a modification to the design described previously [102]. The inductively coupled NMR circuit enables switching between different NMR frequencies by simply replacing the NMR coil, and also allows for coils with different geometries to accommodate different sample shapes and sizes. For example, the Alderman-Grant ^{1}H coil can be replaced with a 2-turn saddle coil for X channel detection (^{13}C, ^{27}Al, ^{7}Li, etc.). To perform CW EPR, the NMR probe module is replaced with an EPR probe module that consists of a solenoid field modulation coil, wound with 100 turns of 30 AWG magnet wire on an 11 mm outer diameter (O.D.) quartz tube, in order to provide B_0 field modulation for CW EPR detection (Fig. 2e). It is important to note that the configuration of the probe insert described above corresponds to a non-resonant mode of MW excitation of the sample.

2.3. MW bridge support structure

The support structure for the MW bridge is mounted on top of an optical table (RS 1000™, Newport Corp.) to minimize vibrations (although this is not so crucial for MWs in the mm-wave regime, so the optical table can be omitted). The support structure can be constructed in any form and from any non-magnetic material that allows for precise vertical, horizontal, and angular position adjustment of the MW bridge relative to the orientation of the MW waveguide. The current support structure is constructed using T-slotted aluminum extrusions (McMaster-Carr), equipped with sliding rails (McMaster-Carr), to enable lateral movement of the bridge positioned above the superconducting magnet to allow removal of the cryostat and/or DNP probe, and to center the MW beam that couples into the waveguide. Four custom machined actuators mounted on the corners of the support structure are used for fine adjustment of the height and relative angle between the MW bridge and the MW waveguide of the probe insert.

2.4. QO MW bridge

The QO MW bridge consists of a custom machined 39.5" × 34.5" × 0.79" (width × length × thickness) aluminum breadboard for mounting the 200 GHz MW source and various QO components to form a QO circuit. They will be described separately below.

2.5. 200 GHz MW source

The 200 GHz MW source is a MW transmitter system (Virginia Diodes Inc.) consisting of a 12 GHz Yttrium Iron Garnet (YIG)-based synthesizer (Micro Lambda Wireless Inc.) connected to a x16 amplifier-multiplier chain (AMC) that results in a final frequency range

of 193–201 GHz and a MW power output of up to 140 mW. The MW amplitude control is integrated into the system and is controlled using an analog input (0–5 V) from a USB-6001 DAC (National Instruments). The MW frequency of the 12 GHz YIG-synthesizer is controlled by a PC with 1 Hz resolution and <12 ms response time using the Specman4EPR software (Femi Instruments, LLC). The precise amplitude and frequency control of the MW source is a crucial capability for obtaining accurate DNP spectra, power curves, as well as frequency stepped pulsed and CW EPR experiments, as will be demonstrated in Sections 3.1.1, 4 and 5. The final output of the 200 GHz MW source is transmitted through a 12.5 mm I.D. transmission horn to the QO circuit as a linearly polarized Gaussian beam with an 8 mm diameter waist. Additional electronic components for MW manipulation can be introduced between the synthesizer and AMC, such as fast diode PIN switches and phase shifters to perform pulsed EPR operation, including phase cycling capabilities, as will be described in Section 2.7, with EPR results reported in Section 5.

2.6. QO Circuits

A low loss QO system is important to ensure efficient MW transmission to the sample, isolating the reflected signal for EPR detection, and preventing reflected MWs from damaging the transmitter source. Below, we will discuss three different QO circuits (a-c in Fig. 3) that have been employed for either DNP or EPR operations. A detailed analysis of the MW power loss through the QO components in each circuit is described in Section 3.2. In the QO configurations described below and shown in Fig. 3, each cube represents half of the 25 cm focal length (*f*) of the elliptical mirrors used in the system. All QO components described here are purchased from Thomas Keating Ltd.

The first QO circuit we will discuss will be referred to as the *low-loss DNP QO circuit* (Fig. 3a), and is the QO circuit used to obtain all DNP data presented in this article. This represents the simplest QO circuit that correctly focuses the Gaussian beam output of the MW source into a target location—in our case, into the corrugated MW waveguide. As the MW beam leaves the transmission horn of the MW source, the beam diverges, increasing in waist size. To re-focus this diverging beam, two elliptical mirrors (with curvatures corresponding to ellipsoids of revolution) are placed in the path of the beam with distance separations of *f*, 2*f* and *f* where the mirrors are placed 2*f* distance apart, while the MW source transmission horn and the corrugated waveguide are *f* distance away from the first and second mirrors, respectively (see Fig. 3a for illustration). In Fig. 3a, an isolator is included to protect the MW source from being damaged by reflected MW power. The QO isolator consists of a combination of a Faraday rotator, wire grid polarizer and absorber, forming an isosceles right triangle. If the MW source is mounted in an orientation that produces a vertically polarized MW beam (↑ when viewing along the path of the beam), the beam first passes through the horizontal wire grid and is rotated 45° counterclockwise upon passing through the Faraday rotator and proceeds onward. However, if any MW is reflected, the reflected beam, already 45° polarized, will rotate further by another 45° upon its 2nd path through the Faraday rotator to create horizontally polarized (←) reflected beam. This beam is subsequently reflected by the horizontal wire grid into the absorber, thus preventing it from returning to the MW source. The low-loss DNP setup is advantageous for DNP operation due to the low transmission loss (~2 dB, see Section 3.2) of MW, but this circuit

does not separate the reflected EPR signal from the unabsorbed MWs, which would result in a large background noise under EPR operation if EPR signal was measured with a detector in place of the absorber in the isolator.

The second QO circuit is another option for DNP operation, here referred to as the *Martin-Puplett DNP QO circuit* (Fig. 3b). This setup was first presented by Armstrong et al. [93] in the first prototype of the 7 T UCSB DNP system. In the Martin-Puplett DNP circuit the vertically polarized beam exits the source transmission horn and passes through the isolator system, both described earlier, where the polarization is rotated by 45° counter-clockwise. The Gaussian beam diverges after leaving the transmission horn, but is reflected as a collimated beam off an elliptical mirror and sent through a Martin-Puplett interferometer, consisting of a vertical wire grid polarizer that acts as a beam splitter and two roof mirrors that rotate the polarization by 90°. One of the roof mirrors is attached to a micrometer that provides lateral movement to adjust the pathlength between the wire grid polarizer and the movable roof mirror. The polarization of the recombined beam after the interferometer changes as a function of the pathlength difference, so that linear, circular, or elliptical polarization can be selected. The MW beam is then refocused by a second elliptical mirror into the waveguide. While the use of circularly polarized MWs leads to an increased absorption of MWs by the sample [93], theoretically generating 41 % higher MW B_1, and therefore higher DNP enhancement, the difficulty in aligning the roof mirrors can easily result in the misalignment of the two roof mirrors that can cause gross distortions to the Gaussian beam profile and loss in MW power, as will be discussed in Section 3.1.2. This configuration is beneficial if the QO configuration can be optimized, and then not frequently altered. Note that circularly polarized MWs are incompatible with induction mode EPR experiments employed in this article.

The final QO circuit that will be discussed is a *dual DNP/EPR QO circuit* (Fig. 3c). It is the circuit that was used to acquire all EPR data presented in this article. After exiting the MW source transmission horn, the incident vertically polarized MW beam (black arrows) passes through an isolator with the resulting polarization rotated by 45°. Subsequently, a 45° wire grid polarizer is placed after the isolator such that the wires are perpendicular to the E-field of the MW beam in order to allow complete transmission of the beam through the polarizer. The beam is then coupled to the waveguide and propagates to the sample. This should allow for a DNP performance similar to that of the first QO circuit, as well as EPR detection as will be discussed next, while the QO alignment is still simple.

It is illustrative to follow the fate of the MW beam when the same circuit is used for EPR signal detection. The incident linearly polarized beam consists of an equal mixture of left and right circularly polarized MW, of which only one of the circularly polarized MW is resonant with the electron spins in the sample. The partial absorption of MWs by the sample thus results in a reflected MW polarization that is elliptical instead of linear. Hence, the elliptical MWs that travel back along the waveguide and enter the QO circuit again will be split at the 45° wire grid polarizer mentioned before, with the rotated EPR signal reflected into the EPR detection system described below (dashed red arrows), while the remaining linear portion of the MW beam that did not interact with the sample passes through the wire grid polarizer and is dumped into the absorber that is part of the isolator (solid red arrows).

2.7. EPR detection hardware

The *dual DNP/EPR QO circuit* described above enables the redirection of the return EPR signal to the EPR detection system. There are several means of detecting this diverted EPR signal. Here, the Mn^{2+} CW EPR spectrum presented in Section 5.1 was acquired using a zero bias Schottky diode detector (ZBD) (Virginia diodes Inc.), while all pulsed EPR data in Section 5.2 was acquired using the superheterodyne detection (SHDD) scheme. Both detection techniques will be described in detail below.

2.7.1. Zero Bias Detection (ZBD)—The ZBD is attached to the end of a receiver horn that converts any 200 GHz EPR signal into a voltage response. ZBD detection is sensitive only to the amplitude of the incident MW beam, so no phase information is available with this type of detection. The biggest advantages of ZBD detection is its high sensitivity and extreme simplicity of implementation. To cope with the $1/f$ noise in the CW EPR signal detection, typically B_0 field modulation together with lock-in detection is employed for CW EPR experiments. Here the B_0 magnetic field at the sample position is modulated using a 20 kHz sinusoidal current provided by a lock-in amplifier (SR830, Stanford Research Systems), applied to a solenoid modulation coil described earlier (Fig. 2e), to result in EPR signals that are modulated by 20 kHz when detected by the ZBD. The 20 kHz modulated voltage output of the ZBD is filtered, amplified and demodulated using the lock-in amplifier. Since the phase acquired between the incident 20 kHz sine frequency applied to the coil and the signal from ZBD is unknown, two traces in quadrature, both containing signal, are typically acquired. Both lock-in amplifier outputs were digitized by the same USB-6001 DAC (National Instruments) used to control the MW amplitude of the 200 GHz transmitter source described in Section 2.5. To generate a single trace signal, zero order phase correction was applied in signal post processing, by varying the phase angle until one of the traces contains only noise and the other all of the signal. Note that the application of lock-in detection results in the acquisition of a derivative EPR signal. Here, instead of applying a magnetic field sweep, as done for conventional CW EPR detection, we stepped the applied MW frequency to acquire the EPR spectrum. The use of the non-resonant MW excitation (as described in Section 2.2) configuration ensures that the coupling of the MWs to the sample is essentially frequency independent over a sufficiently narrow bandwidth, such as 1 GHz to cover an EPR spectrum. The frequency stepped CW EPR detection is a new capability enabled by the precise frequency control of the solid state MW source available to our system, as described earlier. The results for this type of CW EPR detection are presented in Section 5.1 of the EPR section below.

2.7.2. Superheterodyne phase sensitive detection (SHDD)—An alternative mode of EPR detection is SHDD, implemented here for pulsed EPR experiments. This method is typically employed in conventional high field EPR instruments, since it combines high sensitivity with the added benefit of phase sensitive quadrature detection. Fig. 4 shows a scheme of how phase-sensitive detection using the SHDD scheme is implemented in our system. In SHDD, the MW beam carrying the EPR signal at 200 GHz, is captured by the receiver horn which is connected in place of the receiver horn of the ZBD detector. The 200 GHz signal is routed to a sub-band mixer of a 200 GHz receiver system (Virginia Diodes Inc.) that down-converts the EPR signal into an intermediate frequency by mixing the EPR

signal at frequency F_S (~200GHz) with the reference frequency of the receiver system's internal frequency F_R (~98.5GHz) to obtain a 3 GHz EPR signal (F_S-2*F_R = 3 GHz). The internal frequency of the receiver system is generated in a similar manner as the 200 GHz MW transmitter signal where a ~12 GHz synthesizer, identical to the one used in the transmitter system, generates the frequency of F_R/8, which is subsequently fed into a x8 AMC to arrive at the required reference frequency of F_R. Note that the reference frequency F_R is selected such that the intermediate frequency is always exactly equal to 3 GHz by setting the receiver and transmitter MW (X-band) synthesizers 187.5MHz apart (F_S/16-F_R/8 = 187.5MHz). The 3 GHz EPR signal from this sub-band mixer is mixed again with an intermediate frequency reference at 3 GHz using an IQ mixer to arrive at two quadrature, absorption and dispersion, EPR signals at DC. In the case of pulsed EPR experiments presented here, the EPR signal from the IQ mixer is sent directly to a fast (1 GHz), dual channel digital-to-analog converter (Acqiris; U1082A-002, Keysight Technologies). Depending on the particular experimental needs, the echo signal is digitized, and either the full (2μs) long trace is stored to the computer or the relevant part of the echo is integrated in real time and only the integral value is stored to the computer memory. In case of CW EPR detection using SHDD, one would need to implement two synchronized lock-in amplifiers to demodulated each output of the IQ mixer independently.

The reference 3 GHz signal is created by mixing the outputs of the transmitter and receiver synthesizers, resulting in a 187.5 MHz frequency output from the mixer. This 187.5 MHz signal is subsequently multiplied x16 to arrive at the 3 GHz reference frequency to be inputted into the IQ mixer. A more detailed description of the IF stage showing every electronic component is presented in the Appendix, Fig. A2. Note that such detection scheme involving an IF stage is insensitive to the relative phases between the transmitter and receiver sources, which allows for the acquisition of frequency-stepped EPR spectra if the two sources are stepped synchronously, maintaining the 187.5 MHz frequency difference, as was implemented in the frequency stepped echo detected experiments presented in the Section 5.2. The phase and frequency at each stage in the EPR detection scheme are given in Fig. 4.

2.8. Pulse forming unit

One key benefit of a solid state MW transmitter is the ability to incorporate various MW electronics between the MW source and the AMC to manipulate the MW field. In particular, pulsed EPR ELDOR experiments are of interest for monitoring the electron polarization profile across the inhomogeneously broadened EPR line. The schematics of the pulse forming unit implemented for our spectrometer that enables pulsed EPR and pulsed ELDOR capabilities is presented in Fig. 5.

To allow for ELDOR experiments, a second MW synthesizer (VDI Inc.) equipped with frequency sweep and frequency modulation capabilities was added to the system. A pair of fast (~100 MHz) TTL controlled pin switches, internal to the VDI transmitter system is used to select, at a given instance, between the output of either of the two sources that are connected to the same AMC. In addition, an extra module is added to allow for selecting between 0° and 180° pulses at the main (transmitter source 1) frequency (F_S) to allow for

phase cycling. This extra module contains an SP2T switch (~100 MHz) that allows for the selection of either a direct path to the AMC or a route through a voltage controlled phase shifter; both routes are subsequently combined and fed into the AMC chain. The voltage controlled phase shifter is adjusted such as to provide a 11.25° phase shift at F_S/16 frequency which will result in a 180° phase shift after the x16 frequency multiplication at the F_S frequency. Such a scheme allows for precise MW pulse control with a time resolution of < 10 ns for both F_S and F_{ELDOR} channels, and 0°;180° phase cycling for the F_S channel (in the current implementation, the F_{ELDOR} channel is not coherent with respect to F_S and F_r so no phase cycling capabilities are relevant). It is important to note that this type of operation, in addition to the EPR detection discussed earlier, is currently not possible with a gyrotron MW source.

2.9. Centralized control software

The control and manipulation of the hardware described and interfacing with commercial NMR spectrometer operation requires specialized software. Here, we have identified Specman4EPR software (Femi Instruments, LLC) to be our choice for centralized control of all DNP and EPR hardware, including the synchronization with the NMR spectrometer [101]. Specman4EPR is suitable for these tasks because the software is already configured for performing complicated EPR experiments and interfacing with homebuilt EPR devices. Hence, precise control of the MW source frequency and amplitude, operation of the lock-in amplifiers, digital-to-analog converter (DAC), analog output devices, etc. becomes straightforward. In practice, the ability to automate DNP experiments, such as frequency sweeps and MW power curves, becomes an extremely valuable tool for efficiently exploring various DNP parameters. This software also includes rich capabilities for implementation of complex pulsed EPR experiments, as demonstrated in the type of pulsed EPR experiments shown in Section 5.2.

3. MW source diagnostics

In this section, we describe the diagnostic tools and measurement methods to characterize the *quality of the 200 GHz MW source* by measuring the MW power profile over frequency and time, the Gaussian beam fidelity of the MW beam output, as well as the *efficiency of the MW transmission system* by analyzing the MW insertion losses through the QO and waveguide components of the system. We also introduce an efficient way to measure MW losses within the probe insert inside the magnetic field, in order to align the QO bridge for optimal coupling of the MW to the transmission waveguide of the probe insert. This is done by employing a broadband (UV to mm-wave frequencies) 420M7 pyroelectric detector (Eltec Instruments Inc.) equipped with a 0.177" x 0.177" square lithium tantalate sensing element, termed a pyroelectric detector, mounted at the sample location within the magnet (see Section 3.2.2). This diagnostic process is necessary to provide confidence in attributing any variation in the DNP data to the sample or experimental design, rather than fluctuations in the quality and performance of the MW output.

3.1. Quality of the 200 GHz MW source

The MW power is measured for the low-loss DNP QO circuit using a power meter while the beam profile is measured for the Martin-Puplett QO circuit with a camera, except for replacements shown in the Appendix, Fig. A1(a and d). The detector is a photoacoustic absolute power meter (Thomas Keating Ltd.) that has a working frequency range of 30 GHz to > 3 THz, and the camera a first generation Spiricon pyrocam (Ophir Optonics).

3.1.1. Power meter measurements: MW power over frequency and time—The point of interest here is to determine the MW power profile over (i) frequency, and (ii) time, as these are the two important hardware operation characteristics when measuring DNP spectra or power curves. For example, a typical nitroxide DNP spectrum (shown in Fig. 6) is obtained by sweeping the MW frequency with 50 MHz resolution across a range from 197.00 GHz to 198.80 GHz, and measuring the DNP enhancement after a signal buildup of 60 s at each frequency point (total experiment time of ~37 mins). This means that during such an experiment, the MW power across frequency and throughout the entire experimental time should have as little variation as possible. Using the power meter, we were able to measure the power output as a function of MW frequency (Fig. 6a), as well as the MW power stability over time at a set MW frequency (Fig. 6b). The MW power stability of the solid state source at a set frequency is excellent, with power fluctuations below 0.05% over > 30 hrs of continuous measurement time. This offers confidence in the quality of the data that require long measurement times such as ^{13}C samples at liquid helium temperatures with T_{1n} values typically of a few hours.

The MW power at each frequency across the entire frequency range of our MW source of 193–201 GHz varies between 80–140 mW (Fig. 6a). However, the variation in MW power within the frequency range typically used for measuring DNP spectra of nitroxide radicals across 197–199 GHz is much smaller, namely between 110–140 mW (Fig. 6a, inset). For comparison, the state of the art gyrotron output would vary from ~5–35 W across a 3 GHz bandwidth [72]. If necessary, the MW power can also be digitally controlled to provide a leveled output power over the desired frequency range, with a digital calibration of the MW power output vs. attenuation to achieve a flat power profile across frequency. Currently, the majority of our DNP MW frequency profiles have been taken with constant applied voltage attenuation, which results in a 20–30 mW power output variation across our working nitroxide frequency range. Instead, when frequency-dependent attenuation is applied to maintain a constant MW power output, a variation of only < 5 mW is registered across the entire 1.8 GHz frequency range relevant for acquiring DNP spectra of nitroxide radicals. Gratifyingly, when comparing both methods of MW attenuation (i.e. constant power vs. constant attenuation), the experimental DNP spectra of 40 mM 4AT at 4 K show little difference in their lineshape (Fig. 7). The small differences are most likely a result of integration error of the NMR spectra, where random noise can contribute to these differences, especially when integrating the unenhanced DNP spectrum with low SNR on the order of 2–5. This hypothesis needs to be carefully tested in future studies

The ability for precise digital control of the MW amplitude and frequency, as demonstrated here, is a key advantage of DNP operation with a solid-state MW source. Additionally, the

large operating frequency range of 8 GHz from 193 to 201 GHz, corresponding to electron g-factors of 1.9562–2.0373, means that not only can the EPR spectra of common organic radical-based polarizing agents such as TEMPO-based nitroxides, BDPA and trityl be accessed without having to sweep the magnetic field, but also that of many half integer transition metal systems. The electron g-factors for the spin ½ transitions of common transition metals can easily shift the resonance frequency significantly compared to nitroxides at a given field, e.g. 0.17 GHz for MnDOTA (g = 2.0014) or 1.12 GHz for Gd^{3+} (g = 1.9918) [13,108]. For transition metals such as Cu complexes (g > 2.1), the needed shift of the B_0 field of 3230 G compared to the resonant field for a free electron cannot be easily achieved, even with a DNP-capable magnet from Bruker Biospin (that offers a total sweep width of ~1500 G). Here, a solid-state MW source is needed to offer the needed frequency shift of 9.49 GHz. The capability of a cryogenic sweep coil with 1500 G sweep width (not available with our DNP system currently) combined with the broadband MW source (10 GHz, yielding an equivalent of 2850 G) can achieve an equivalent total sweep width of 4350 G, while the capability of a room temperature sweep coil with 400 G sweep width can achieve an equivalent total sweep width of 3250 G. While the absolute power output of the current solid-state sources is still limiting in the quest to achieve optimum DNP performance at higher temperatures, the replacement of the current MW source with a higher output MW source or the implementation of higher power amplifiers in the future will not compromise the current versatility and diagnostics measurements available with the versatile QO DNP circuit as presented here.

3.1.2. Pyrocam measurements: MW beam image profiling—The integrity of the Gaussian profile of the MW beam is crucial, so that the polarization of the beam can be manipulated correctly with QO positioning and alignment, the power loss minimized as the beam travels through different QO components, and the MW-induced excitation ensured to be spatially even across the sample area when the beam is incident on the sample. The Gaussian fidelity of the MW beam, characterized by the size, Gaussian shape, and relative power of the MW beam, is imaged at every position along the transmission path of the MW beam of the low loss DNP QO circuit (Fig. 3a). At the immediate output of the MW source (i.e. at the transmission horn) we measured the MW beam to be circular with a Gaussian profile (Fig. 8a). This Gaussian profile is maintained for the entire path of the MW, as verified with the focused MW beam at the end of the QO circuit, as shown in the position of the power meter in the Appendix Fig. A1a.

We also performed the same beam profiling for the Martin-Puplett DNP QO circuit (Fig. A1d), which is the DNP circuit used in the first prototype of this DNP system [93]. In this circuit, the Martin-Puplett interferometer was used to choose between linear and circular polarization, where the use of circular polarization was found to provide a maximum of 28% higher DNP enhancement compared to linearly polarized MWs. However, in the Martin-Puplett DNP QO circuit, detecting the beam quality after manipulation by the Martin-Puplett interferometer reveals that the Gaussian beam becomes distorted by even a 0.5° vertical misalignment of the movable roof mirror (Fig. 8b). A complete discussion of the QO analysis of the Martin-Puplett interferometer circuit and elucidation of MW power losses due to roof mirror misalignment in this circuit can be found in the Appendix (Section 10.4).

The distortion of the beam also results in an overall reduced MW power—such complications do not occur with the low-loss QO circuit. Equipped with this knowledge, we chose the low-loss DNP QO circuit as our reliable base setup to acquire all the DNP data presented in this article, until we have an operation in place where the positioning of the interferometer can be finely adjusted to provide circular polarization and its configuration not altered—currently, we are switching between different QO circuits.

3.2. Efficiency of the MW transmission system

Power analyses of the transmission system (QO MW bridge, waveguide, waveguide extension) were performed by comparing the direct MW power output of the source to the resulting MW power after passing through each transmission system component. In this section, we will also discuss the MW alignment process of the MW bridge in relation to the corrugated waveguide of the DNP probe as measured by the pyroelectric detector within the magnet (see details below), where the MW bridge alignment is critical for minimizing MW loss due to imperfect coupling of the MW beam into the waveguide.

3.2.1. Insertion losses of QO components—The QO circuits are examined in detail where the measured insertion losses of all the QO components (including the MW waveguide) are tabulated in Table 2, while the theoretical and measured total loss of the different QO circuits are presented in Table 3. The procedure for determining the insertion loss for each QO component is detailed in Appendix 10.1, whereby all insertion loss measurements are performed with the power meter. When analyzing the insertion losses of the QO components, we find that the measured loss associated with the Martin Puplett interferometer when linear polarization is chosen is largest (3.3 dB) compared to the other QO components (Table 2), confirming that the MW beam distortion captured by the pyrocam contributes significantly to the MW power loss, given that the interferometer components (roof mirrors, wire grid polarizer) are otherwise essentially lossless (<0.05 dB). The insertion loss is only measured for linear polarization since the rotated polarization induced by the interferometer makes it very difficult to obtain polarization parallel to the bridge for an accurate power reading (i.e. the power meter cannot measure circularly polarized MWs accurately). The loss associated with the flat mirror was experimentally determined to be dependent on the placement of the mirror, which corresponds to positions where the MW beam is diverging or converging. This is contrary to QO theory that flat mirrors should have negligible loss, which indicates that there could be imperfections in the smoothness of the flat mirror. The observation of this position-dependent power loss associated with the flat mirror is also present in the different QO schemes. Aside from these losses that are not intrinsic but solvable, the isolator and waveguide have losses of 1.3 dB and 0.45 dB, respectively, which is consistent given the expected losses of ~1 dB for a Faraday rotator that is part of the isolator. The measured power losses for all the QO components will allow us to determine the total loss of each QO circuit, as will be analyzed next.

In Table 3, the theoretical loss associated with all QO circuits, listed earlier in Fig. 3, were calculated from the measured insertion losses (Table 2) and compared to the measured power loss values obtained with the pyroelectric detector mounted at the sample position

inside the magnet. The MW source is digitally modulated at 20 Hz with a SR830 lock-in amplifier (Stanford Research Systems) so that the power detected by the pyroelectric detector can be converted into a voltage response measured by the same lock-in amplifier. In order to obtain an accurate comparison between the voltage reading of the pyroelectric and the direct MW power reading of the power meter, a linear calibration curve correlating the two values was made. For the dual DNP/EPR QO circuit, the power meter was used to obtain the actual loss at the position of the EPR detector.

From the theoretical loss calculations, the low-loss DNP circuit provides the least total MW power loss (2 dB) compared to the Martin-Puplett circuit (5 dB) or the dual DNP/EPR circuit (3.7 dB) at the sample position. When the insertion loss through the entire QO circuit is measured, the measured values are consistent with the predicted theoretical values within error. Taken together, the dual DNP/EPR QO circuit is the best compromise between low power loss and the access to combined DNP and EPR capabilities. In the future, we will further characterize the performance of the dual DNP/EPR QO circuit to that of the low-loss DNP QO circuit, by comparing experimental DNP enhancement and EPR data.

3.2.2. MW bridge alignment and MW characterization of probe insert—After the MW beam exits the MW bridge and is coupled into the top of the waveguide, it travels downward into the magnet through the corrugated waveguide to the sample. The alignment between the MW bridge and the waveguide is an extremely important parameter, as this critically determines the degree of MW power loss through the waveguide. With good alignment, the total MW loss can be kept to a total of 2 dB for the low-loss DNP QO circuit, in which there is virtually no loss through the waveguide. To perform MW alignment, we found that maximizing the reading of the pyroelectric detector (described in Section 3.2.1) mounted at the sample position inside the magnet is the most efficient and accurate empirical method. To optimize MW alignment, the position of the MW bridge is varied vertically, laterally and angularly with respect to the waveguide. The pyroelectric detector reading also provides a relative measure of the amount of MW power incident at the sample, when referencing the pyroelectric read-out voltage values to the calibration of the power meter reading.

Another advantage of using the pyroelectric detector at the sample position is that losses through different waveguide components mounted as part of the DNP probe can be separately determined, such as the four different waveguide extensions shown in Fig. 2c, with insertion losses tabulated in Table 4. Two of the waveguide extensions are smooth walled and machined out of solid copper or magnesium-stabilized zirconia (material from International Ceramic Engineering, machined by Thomas Keating Ltd.). The other two are corrugated thin films of gold epoxied onto two different plastic supports. For the smooth walled extensions, the zirconia waveguide extension incurs a surprisingly large insertion loss of 7.46 dB (82 % MW power loss), while the simple copper waveguide extension transmits the MW power between the exit of the waveguide taper and the sample without any measurable loss. The performance of the easy-to-machine smooth copper waveguide is comparable to a corrugated waveguide extension optimized for MW transmission, and was ultimately used to acquire all the DNP data presented here. However, strong radiofrequency NMR pulses may cause eddy currents when the NMR coil is positioned too close to the solid

copper waveguide extension—a problem that we did not encounter in our setup so far. With the same test, we were able to verify that one of our corrugated waveguide extensions, which had previously been shown to be low-loss [50,93,102,103] had been damaged as there was a measurable insertion loss of 1.46 dB (20 % loss in MW power), previously not observed. To verify the visible damage to the corrugated gold thin film was responsible for the loss, the MW loss through this damaged waveguide extension was compared with a pristine waveguide extension with the same construction, except on a plastic support with a high ^{1}H NMR background signal. Indeed, the pristine waveguide extension did not exhibit any insertion loss, verifying our hypothesis that the discussed insertion loss is caused by mechanical damage to the thin film corrugation of the waveguide extension. The waveguide extension is very important because it is the last length of travel before the MWs exit into free space. Thus, the function of the waveguide extension is to contain the MWs for as much distance as possible before arriving at the sample, but without interfering with the NMR probe performance. Since, the NMR probe is situated at the end of the waveguide extension, it is important to consider the effect of NMR background signal from the plastic support and material used to fabricate the waveguide extension. From the four waveguide extensions examined here, the smooth copper waveguide provides the best MW containment and lowest ^{1}H background NMR signal.

Here, it is important to consider the effect of substituting a corrugated waveguide extension with a smooth walled waveguide extension. By changing from a corrugated waveguide to a smooth walled waveguide, the wavefront of the HE_{11} mode transmitted in the corrugated waveguide will be distorted [104,106]. In addition to the power losses induced by the coupling efficiency between perfectly aligned smooth walled and corrugated waveguides, any misalignment of the waveguide and the waveguide extension can result in mode conversions, such as axial offsets, tilts, and abrupt changes in radius [106,107]. The abrupt change in radius becomes significant if one was to minimize modal mismatching between the two waveguide types, where the smooth walled waveguide would have to have a radius that is 0.842 times smaller than the corrugated waveguide (see discussion in 2.2). Besides the mode conversions this would cause, there would also be significant back reflections due to the discontinuity in the waveguide radius [106], which is extremely disadvantageous for EPR operation. The attenuation caused by using a smooth walled waveguide extension is considered negligible over the 43 mm length of the extension. Thus in order to maximize power transmitted through the waveguide extension and minimize reflections for EPR operation, a 5.3 mm ID was used for both corrugated and smooth walled waveguide extensions. The slight power loss due to mode conversions between corrugated and smooth walled waveguides will have a minimal impact on DNP operation, since at this time we are primarily interested in the power transmitted and not the wavefront or mode transmitted. However, this will have a more significant impact for EPR operation due to the power losses from the modal mismatches by switching between corrugated and smooth walled guides becomes more relevant for the inherently low EPR signal. Finally, the distorted wavefront may not uniformly irradiate the sample's surface area, which would have the greatest impact on EPR detection. Considering MW transmission and low ^{1}H background NMR signal, the smooth walled copper waveguide was used for the rest of data presented here. In the future,

we will employ a thin metal corrugated waveguide mounted on a ^{1}H background free dielectric support, or a corrugated copper waveguide.

4. DNP data reliability and power saturation behavior of DNP at different temperatures

The ultimate manifestation of the stability and robustness of an instrument is the experimental output. We show that the DNP spectra, which is the DNP enhancement as a function of MW frequency, is reproducible within a span of 3 years between two data sets acquired with two different QO circuits (Fig. 9), while employing the same sample and experimental conditions. Within those 3 years, the entire instrument was disassembled and moved to a different location, and the MW source (in particular the AMC) reconfigured and upgraded from a 70 mW output to a 90–140 mW output. Remarkably, the modifications to the MW system apparently did not compromise the integrity and quality of the DNP data, supporting that the DNP spectrum presents a relevant intrinsic characteristics of the sample. Once again, as explained in Section 3.1.1 the small variations in intensity are most likely due to signal integration error rather than hardware variations.

One concern when working with a solid-state diode MW source, with power on the order of 100 mW, is that the ultimate DNP enhancement will be limited by the MW source output power. In order to determine whether and under what conditions this is the case, the DNP signal enhancement was measured as a function of MW power—this type of plot is referred to as a DNP power curve. Fig. 10 presents DNP power curves of frozen solutions containing 4AT at 40 mM concentration, acquired at 4, 6, and 20 K temperatures. At 4 and 6 K, the DNP power curve showed an increase in DNP enhancement with increasing MW power, which eventually reached a maximum value, and then decreased as the MW power is increased further. We discussed in our earlier study that this decrease in DNP enhancement above a certain MW threshold power to be due to oversaturation, in which the maximum polarization differential between pairs of dipolar coupled electron spins with a frequency difference corresponding to the nuclear Larmor frequency are diminished, due to significant saturation of the EPR spectrum beyond an optimum threshold [50]. Supporting ELDOR data that verifies the dramatic EPR saturation under the relevant conditions here are presented in the Section 5.3.

The observation of oversaturation under our experimental conditions has important implications: it means that for a 40 mM 4AT sample, we have sufficient MW power at 4 and 6 K to drive the system to its maximum enhancement value, suggesting that we can extend the operation of this sample to a higher temperature, especially when frequency modulation is employed, without being MW power limited. At 20 and 90 K, the power curves do not indicate an area of oversaturation, but is seen to reach a plateau with increasing MW power. When comparing the 94 and 18 fold enhancement values at 20 K and 90 K, respectively, in which we say we are not power limited, to literature DNP data at similar or higher temperatures, the reader is reminded that the measurements presented here rely on mono-nitroxide radicals of 4AT that likely offer similarly low enhancement performance even with commercial DNP hardware. The absence of an oversaturation regime when increasing the temperature to 20 and 90 K is likely due to the large drop of the integral saturation factor,

S_{int}, empirically defined in our previous publication [50] as T_{1e} multiplied by the electron flip-flop rate, W_{flipflop}, where a drop in S_{int} of at least 3 fold occurs at 20 K.

The effect of MW-driven saturation of the EPR spectrum on the DNP mechanism can also be examined by analyzing the DNP spectra. The dominant DNP mechanism is characterized by the peak-to-peak frequency difference between the positive and negative enhancement extrema (Δ_{DNP}), as tabulated in Table 5. In a dilute solution of nitroxides, where the dominant spin polarization transfer is between a single electron and nuclear spins, the SE mechanism dominates and yield $\Delta_{\text{DNP}} = 2\omega_n = 600$ MHz (for ^{1}H at 7 T). On the other hand, the CE mechanism (including the indirect CE, iCE) dominates when the nitroxide concentration is increased to approximately > 10 mM to increase the probability of pairs of dipolar coupled nitroxides with a Larmor frequency difference corresponding to ω_n, and yields $A_{\text{DNP}} \approx 2\omega_n$, while Δ_{DNP} lies within the width of the EPR spectrum. For all temperatures studied here and at an electron spin concentration of 40 mM, Δ_{DNP} lies between 400 and 450 MHz, depending on the temperature (Table 5), which is characteristic of a CE-dominated mechanism, given that the EPR spectral width spans 1 GHz, base-to-base. The observation that Δ_{DNP} decreased to 400 MHz at 20 and 90 K, from 450 MHz at 4 and 6 K (Fig. 11 and Table 5), is consistent with the observation made earlier at 3.4 T that Δ_{DNP} decreases with increasing temperature [51,52]. We hypothesize that the decrease of Δ_{DNP} at higher temperatures is partly (if not entirely) caused by l ess efficient saturation of the nitroxide EPR line, which is in line with recent electron depolarization experiments and simulations by Hovav et al. [49] Further studies will be performed in the future where the power dependence of the DNP spectra and EPR saturation profile will be examined at different temperatures. Nonetheless, it should be made clear that our hypothesis does not exclude the possibility of other factors affecting the temperature-dependence of the DNP mechanism, such as the weighting of the DNP mechanisms that may change with S_{int} for the EPR spectrum.

5. EPR experiments

In this section we present results from several EPR experiments, both in pulsed and CW modes of operation that showcase the EPR capabilities of our current 200 GHz dual EPR/DNP setup.

5.1. Frequency stepped CW EPR

To illustrate the CW EPR capabilities of our 200 GHz QO EPR system, we performed room temperature EPR experiments with ZBD on a modeling clay sample containing Mn^{2+} (S=5/2; I=5/2) typically employed in testing EPR instrument performance. Fig. 12 shows an overlay of the two CW EPR spectra of Mn^{2+} containing clay sample. The spectrum shown in black was acquired with our 200 GHz QO DNP/EPR spectrometer using ZBD and stepping the frequency through the EPR spectrum. While stepping the frequency through the EPR spectrum is not a conventional EPR detection method, this method has been attempted by several groups with great success [109,110]. This spectrum is overlaid with the spectrum shown in red after correct scaling, which was obtained with a 240 GHz EPR spectrometer in the laboratory of Professor Mark Sherwin (UCSB) [97,111] using conventional field-sweep CW EPR detection. The field swept spectrum was converted to frequency units and inverted

relative to its center, and then the center frequency subtracted from both spectra to allow for alignment of the frequency axis. Gratifyingly, the two spectra are in excellent agreement with one another. Both spectra show the typical Mn^{2+} sextet due to hyperfine interaction with the nuclear spin of ^{55}Mn (I=5/2). The six lines are equally spaced with 266 MHz separation, in good agreement with values typically obtained for Mn^{2+} [112]. Slight differences in the intensity of the two leftmost lines between the two spectra are attributed to the presence of residual standing waves in the QO system or to variations in incident MW power in the 200 GHz system that likely affects the effective B_1 field at the sample position in a MW frequency-dependent way. Fine tuning of the unique frequency stepped EPR experimental setup and dealing with these complications that are unique to frequency stepped EPR approach is work in progress.

5.2. Pulsed EPR

To demonstrate pulsed EPR capabilities of our system we show the results of several standard pulsed EPR experiments in Fig. 13. Fig. 13a shows the overlay of the echo detected *frequency stepped* spectrum of P1 (nitrogen) centers of a type 1b diamond acquired on our 200 GHz system (black trace) with the echo detected *field swept* EPR spectrum (red trace) acquired at 240 GHz in the laboratory of Professor Mark Sherwin (UCSB), where both spectra were acquired at room temperature for the same sample. The two spectra show the characteristic triplet due to the hyperfine interactions of the unpaired electron in the P1 center with ^{14}N. Similar to what is previously observed in the CW EPR spectra comparison (Fig. 12) between the two systems, the line positions and linewidth are consistent between the two, while the line intensities are not. Again, this is attributed to the presence of frequency dependent standing waves in the 200 GHz system and to variations of incident power across the frequency range used to acquire the EPR spectrum.

One of the strengths of pulsed EPR, in relation to elucidating DNP mechanism, lies in its ability to directly probe the relaxation properties of the electron spins participating in DNP. Accordingly, we demonstrate relevant pulsed EPR capabilities by measuring the phase memory time, T_M, (Fig. 13b) using a two-pulse (t_p-τ-t_p-τ-echo) spin echo pulse sequence (see Fig. 13b inset) where τ is varied, and the electron spin-lattice relaxation time, T_{1e}, (Fig. 13c) using a three-pulse saturation recovery (t_{sat}-t_d-t_p-τ-t_p-τ-echo) pulse sequence (Fig. 13c inset), where t_d is varied. Both experiments were carried on the central line of the P1 center triplet of the same diamond sample at room temperature (290 K). Both curves could be satisfactorily fitted with a single exponential, and the obtained values of T_M = 965 ns and T_{1e} = 1.6 ms are in good agreement with measurements performed using the 240 GHz EPR setup in the Sherwin group at UCSB on the same diamond sample.

Similar to NMR, nutation experiments by pulsed EPR can be used to directly determine the strength of the oscillatory magnetic field B_1 at the sample position. A three pulse nutation experiment (t_{sat}-t_d-t_p-τ-t_p-τ-echo) (Fig. 14a inset) where the length of the first "t_{sat}" pulse is varied was used to probe the B_1 strength. The experiment was carried out at 4 K and 7 T of 40 mM 4-amino-TEMPO radical in a frozen glass of 60:30:10 v% d_8-glycerol:D_2O:H_2O, using the full available MW power of ~130 mW and at F_S = 197.925 GHz. The EPR nutation curve is presented in Fig. 14a, with the nutation trace showing a decaying

oscillation typical of echo detected nutation experiments, where the decay of the oscillation is attributed to inhomogeneous B_1 field distribution over the sample. The first minimum of the nutation curve occurs at 850 ns (black arrow in Fig. 14a) corresponding to a nutation frequency of ~0.6 MHz, and a conversion factor of $1.66 \frac{MHz}{\sqrt{Watt}}$. This $B1$ field at 7 T is consistent with non-resonant MW excitation schemes used for other ~200 GHz EPR setups where ~100 mW output MW sources result in several hundred nanosecond $\pi/2$ pulses [113,114]. For MAS-type DNP setups with non-resonant MW excitation, much higher MW powers might be needed, such as 17 W to produce a 0.84 MHz B_1 strength, as recently calculated by Barnes et al. for a gyrotron powered setup [79].

5.3. Pulsed ELDOR

In our recent publication [50] and in the DNP power curves presented above, we described the observation of oversaturation at 4 K and 7 T in a frozen glass with high (~40 mM) nitroxide spin concentration. Our dual DNP/EPR spectrometer allows for the acquisition of explicit ELDOR experiments, in which the electron depolarization is monitored using the "probe" echo pulse sequence following prolonged MW irradiation, emulating CW DNP irradiation at the F_{ELDOR} frequency. The overall pulse sequence of the ELDOR experiment $t_{sat}(F_{ELDOR}) - t_d - t_p(F_S) - \tau - t_p(F_S) - \tau$-echo is shown in the insert of Fig. 14b. In this experiment the echo intensity at Fs frequency is monitored as function of the F_{ELDOR} frequency. An example of such ELDOR spectrum acquired at 4 K on the 40 mM 4AT radical in d_8-glycerol:D_2O:H_2O (60:30:10 v%) is shown in Fig. 14b. Here the detection F_S frequency was set to the maximum EPR signal of the nitroxide spectrum at 197.925 GHz and the F_{ELDOR} frequency was varied across the whole nitroxide spectrum between 197.3–198.4 GHz. The spectrum shows full depolarization at $F_{ELDOR} = F$s with a significant depolarization observed up to $F_{ELDOR} = 197.5$ GHz on the low frequency and $F_{ELDOR} = 198.3$ GHz on the high frequency side of the spectrum, spanning almost 1 GHz. Such broad depolarization pattern is attributed to a strong spectral diffusion previously reported for nitroxide radicals at similar concentration as measured by similar ELDOR experiments at 95 GHz [49], but at much lower temperatures of 4 K where the effect of EPR saturation will be greater, in part owing to long T_{1e}. It was demonstrated that from a series of such ELDOR spectra acquired for several "probe" F_S frequencies, it is possible to reconstruct the saturation pattern of the EPR spectrum under DNP conditions—which is drastically different from any normal EPR operating conditions. These type of experiments will reveal the extent (width and depth) of saturation under conditions where maximum DNP enhancement or oversaturation occurs in systematic future studies. The benefit of ELDOR measurements to help rationalize DNP mechanisms under static conditions has been demonstrated recently at 3.3 T and 95 GHz EPR frequency by Hovav et al. [49,54]. However, ELDOR under CW DNP conditions and at higher magnetic fields such as our 7 T system is not reported to date. Taken together, we have demonstrated here that the versatility of our combined DNP/EPR approach that relies on the frequency-tunable and amplitude modulation capable solid state MW source and QO transmission enables a variety of pulsed EPR experiments, and that many more variations of EPR experiments can be implemented with ease.

6. Outlook

The implementation of dual DNP/EPR detection in this article is a first step toward rational prediction of DNP performance through a more in-depth and precise understanding of the effect of all relevant DNP parameters, including but not limited to EPR and NMR relaxation timescales, temperature, magnetic field, and microwave power. With a dual DNP/EPR setup, all these relevant parameters can be explored with the aid of automated experiments, especially for time consuming measurements. Moreover, additional EPR capabilities can be added on such as ENDOR and DEER as powerful tools for further probing the e-e and e-n interactions—an effort that will be pursued in the future.

In forthcoming publications, with the newly implemented EPR abilities, we will attempt to unravel the intricacies of DNP processes by systematic measurements of temperature dependent DNP parameters (T_{1e}, T_M, T_{1n}, T_{2n}, T_{SD}, DNP, DNP enhancement) in an effort to improve DNP simulation abilities and to understand the DNP oversaturation process. It is also desirable to extend these type of measurements to different systems other than frozen glass solutions in order to analyze the impact of different materials and biosolids structures on DNP performance. We believe the increased ability and efficiency to explore the DNP parameter space will contribute to the understanding of DNP mechanisms, and thus predictability of DNP performance. This will be an important step towards the wider dissemination of DNP as a staple magnetic resonance characterization technique.

7. Materials and experimental details

7.1. Sample preparation

A solid powder of 4-amino TEMPO free radical (4AT) (Sigma Aldrich) was dissolved in a 5:4:1 volume ratio of d_8-glycerol:D_2O:H_2O and diluted to a concentration of 40 mM. For DNP spectra and power curve measurements, 40 μL of the nitroxide solution is then pipetted into a 7 mm outer diameter and height, 5.3 mm inner diameter cylindrical PTFE sample holder for our homebuilt 300 MHz NMR probe [102]. These samples were then cooled down to various temperatures inside a custom Janis continuous-flow STVP-NMR cryostat.

For room temperature (290 K) CW EPR measurements, modeling clay (Plastalina, Van Aken, hobby lobby) containing Mn(II) was used as received, smearing ~3 mg onto a silver coated quartz mirror (Thor Labs) and the prepared quartz mirror is subsequently placed at the exit of the waveguide extension described in the main body of the article. Room temperature pulsed EPR measurements of P1 centers in a type 1b diamond sample were performed in the same manner where a 3×3 mm square diamond sample was adhered to a silver coated quartz mirror using Apiezon N-vacuum grease (M&I Materials).

For pulsed EPR measurements of 4AT a concentration of 40 mM was prepared in a solvent of 60:30:10 v% d_8-glycerol:D_2O:H_2O and 6 μL of the resulting solution was placed in a Teflon sample cup with ~3.5 mm inner diameter. The sample cup was placed inside the copper waveguide extension with a silver coated quartz mirror below the sample in order to maximize the B_1 field at the sample. All pulsed EPR measurements on this sample were

performed at 4 K. Experimental parameters of the pulsed EPR measurements are described in the relevant sections of the text body (Sections 5.2 and 5.3).

7.2. DNP measurements

All ^{1}H NMR-DNP measurements were performed with an inductively coupled Alderman-Grant probe as described in our previous publication [102] or a modification thereof. All DNP experiments presented here were performed at 4–90 K and 7 T, using a 300 MHz ^{1}H NMR rf frequency channel of a Bruker Avance D300WB console. A standard saturation-recovery pulse sequence ending with a solid-echo detection was used to detect NMR signals. A DNP frequency spectrum at maximum MW power is obtained at 4,6, 20 and 90 K by measuring the NMR signal enhancements, s(v), at different MW irradiation frequencies (v), from 197.000 to 198.800 GHz, at 60 s of signal build up time. The value for $\varepsilon(\mathbf{v})$ is quantified by taking the ratio of the area of the NMR signal with (S_{DNP}) and without (S_{NMR}) MW irradiation [$\varepsilon(v) = S_{DNP}/S_{NMR}$]. A DNP power curve at 60 s DNP signal buildup time is obtained by measuring $\varepsilon(\mathbf{v})$ at one frequency, generally the frequency that offers maximum positive enhancement (typically 197.700 GHz here), as a function of MW source power by stepping the voltage applied to the PIN switch that provides attenuation to the MW source. This 60 s DNP signal is then compared with a thermal equilibrium signal (measured typically at $3*T_{DNP}$), and extrapolated to steady state to obtain the final DNP enhancement value via the saturation recovery equation $M_Z(t)= M_{eq} [1-\exp(-t/T_{DNP})]$, where M_Z is the magnetization at 60 s delay, $t = 60$ s, and T_{DNP} is measured using saturation recovery for all relevant temperatures.

7.3. EPR relaxation measurements at 8.5 T

Pulsed EPR measurements were carried out at 240 GHz using a low power (~30–50 mW) solid state source, developed as the staging instrument for a Free Electron Laser-powered EPR spectrometer [97]. Sample volumes of 5 to 10 μL were placed in a Teflon sample cup with a ~3.5 mm inner diameter and 5 mm height, and loaded into the waveguide that is placed in a custom Janis STVP-NMR continuous-flow cryostat pre-cooled to 230 K.

A 650 ns-τ-750 ns-τ spin-echo pulse sequence was used in measurements of the phase-memory times (T_M), at the magnetic field that yielded the maximum echo intensity for the 4-AT or TOTAPOL spectrum. The resulting echo decay was fit with a stretched exponential decay $\exp(-2\tau/T_M)^{\alpha}$, whereby $\alpha = 3/2$ was empirically chosen and verified for a frozen glycerol-water glass nitroxide sample system [115]. The uncertainties in T_M are estimated as ±5% of the measured values from repeated measurements. Measurements of the electron spin-lattice relaxation times (T_{1e}) were carried out with a 3-pulse saturation sequence of the form: saturation-T-650 ns- τ –750 ns- τ. Where T is the recovery delay and τ is the inter-pulse delay. The saturation pulse length was varied until no change in the signal buildup was observed by lengthening the saturation pulse, which ranged from 10 to several hundred milliseconds. The experimental curves were fit by a bi-exponential buildup of the form,

$y=y_0[1 - A\exp(-\dfrac{t}{T_{SD}}) - B\exp(-\dfrac{t}{T_{1e}})]$, where T_{SD} is the faster time constant corresponding to the spectral diffusion process and T_{1e} the slower time constant.

8. Conclusions

In this perspective article, we have presented an operational dual DNP/EPR instrument and system operating at a B_0 field of 7 T and powered by a solid-state MW source, whose MW transmission, reflection and detection is controlled by a QO MW bridge. The versatility of the solid-state MW source and modularity of the QO transmission system enables the manipulation of the system to perform different types of measurements, such as MW power measurements to characterize the MW source and track the MW power losses across the MW transmission system, acquire DNP spectra and power curves, and carry out CW and pulsed EPR measurements. The MW diagnostic measurements revealed the MW power stability over hours/days, and a low loss DNP configuration of 2 dB from the MW source to the sample. Using the reliability of the MW source, we measured the temperature dependence of the DNP power curves and DNP spectral width. We found that the narrowing of the DNP spectra at higher temperatures above 6 K is simultaneously accompanied by the disappearance of an oversaturation regime observed at 4 and 6 K, suggesting that MW power saturation plays an important role in determining the DNP spectral width and shape. The disappearance of the oversaturation regime can be explained by a 3 fold decrease in S_{int}. Furthermore, using this dual DNP/EPR spectrometer we demonstrated the ability to acquire frequency stepped pulsed and CW EPR spectra that are in good agreement with the more common field swept CW EPR spectra. The implementation of pulsed EPR also enables insightful ELDOR experiments that will facilitate the understanding of DNP processes such as DNP oversaturation, and improve the ability to predict DNP performance via fitting of DNP spectra and power curves. The dual EPR/DNP capabilities will greatly increase the ability to explore the DNP parameter space. In summary, we have demonstrated that the reliability, versatility, and modularity of our dual DNP/EPR instrument is an excellent configuration to explore the DNP performance of different samples and experimental conditions in order to study the spin physics of DNP.

Acknowledgments

Appendix

10.1. Insertion loss analysis of individual QO components

The MW source output power was determined with the simple 2-mirror set-up is shown in Fig. A1a. Fig. A1b–e shows the incorporation of isolators, waveguide, flat mirrors, and interferometer, into the simple 2-mirror set-up. For the accurate testing of the losses associated with these QO components it is imperative that the E-field is parallel to the plane of the bridge and at Brewster's angle (55.5°) to the detection film of the power meter when using the power meter, such that reflections are minimized, which allows for a frequency independent absolute power calibration. This is why additional Faraday rotators or the angle of the source itself was altered in order to achieve the required orientation of the E-field. The power losses for each of the QO configurations shown in Fig. A1b–e was then compared to the power measured for reference QO configuration Fig. A1a to arrive at the loss associated with each QO component.
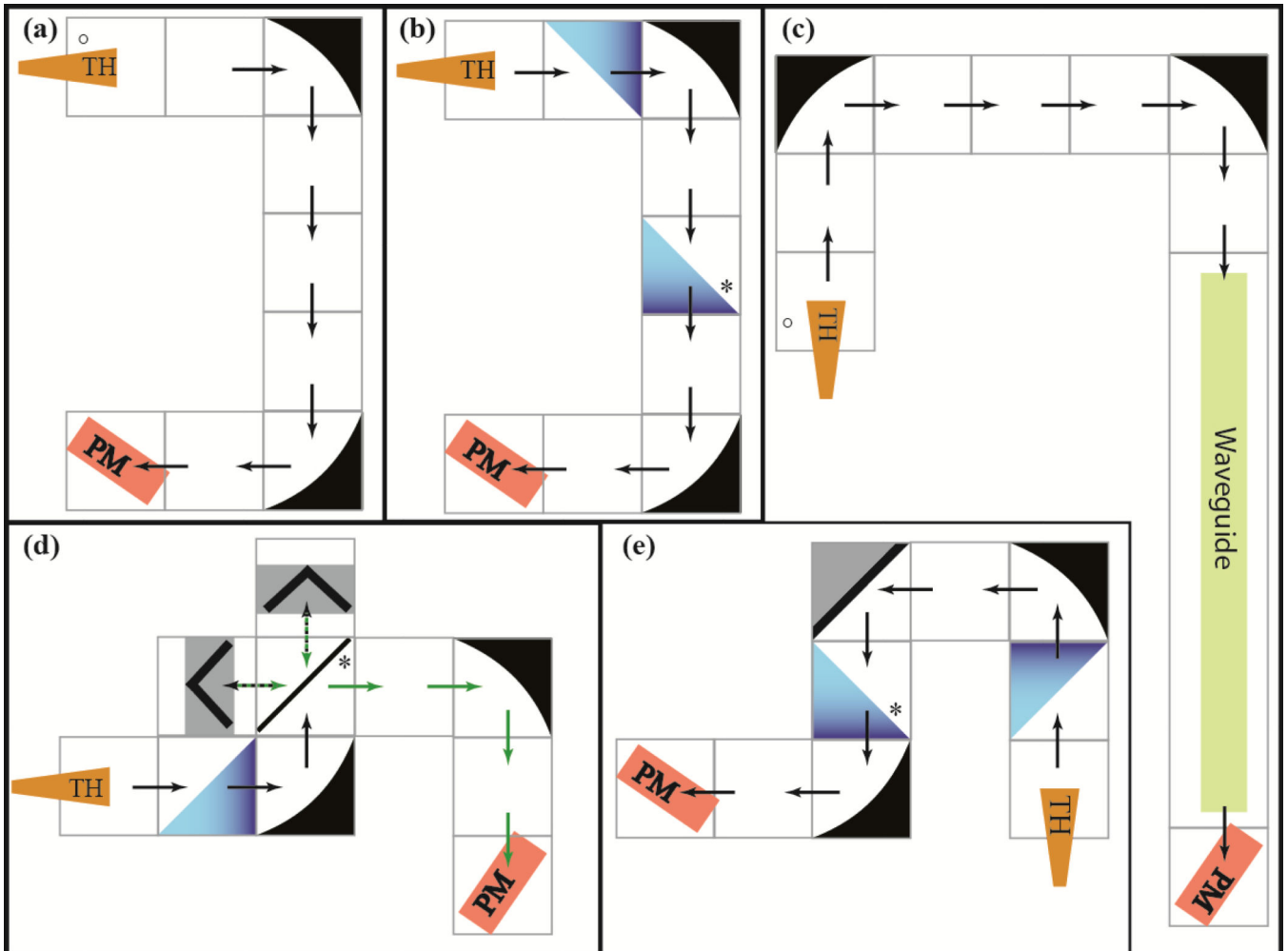

Figure A1 Schematics of quasi-optical set-ups for power analysis. a) A simple 2-mirror set-up; reference configuration. b) A simple 2-mirror set-up with two isolators; for measurement

of isolator insertion loss c) Simple 2-mirror set-up with waveguide; for measurement of waveguide insertion loss d) 2-mirror set-up with isolator and interferometer; for measurement of Martin-Puplett interferometer insertion loss e) Three mirror set-up with a flat mirror between the two ellipsoid mirrors; for measurement of flat mirror insertion loss. ° indicates the source is oriented such that the E-field is horizontal; otherwise, the source is oriented for a vertical E-field. Each tile represents a distance of 12.5 cm (f/2). * indicates a 45° wire grid polarizer. PM denotes the power meter.

10.2. Details of the intermediate frequency (IF) stage of the SHDD system

Fig. A2 below shows all the MW electronic components used in the SHDD system's IF stage to generate a reference 3 GHz IF signal. The 12 GHz synthesizer outputs of the VDI transmitter and receiver sources are shown on the top left corner. The frequencies of the two synthesizers are set 187.5 MHz apart. Consequently a 187.5 MHz frequency is produced after the first mixer (Marki M10616NA). This 187.5 MHz frequency is then amplified and multiplied x16 to 3 GHz (with filters applied to maintain spectral purity). This signal is used to drive the IQ mixer's LO channel. A 3 GHz signal originating from the sub-band mixer of the VDI receiver system is fed into the RF input of the same IQ mixer as described in the main body of the article. Between the receiver system and the RF channel of the IQ mixer, a series of amplifier, isolator, and filter is used to provide a clean 3 GHz signal at the appropriate amplitude for the IQ mixer and protect the receiver system from reflected MW power. The outputs of the IQ mixer provide real and imaginary quadrature DC signals of the EPR signal arising from the sample.
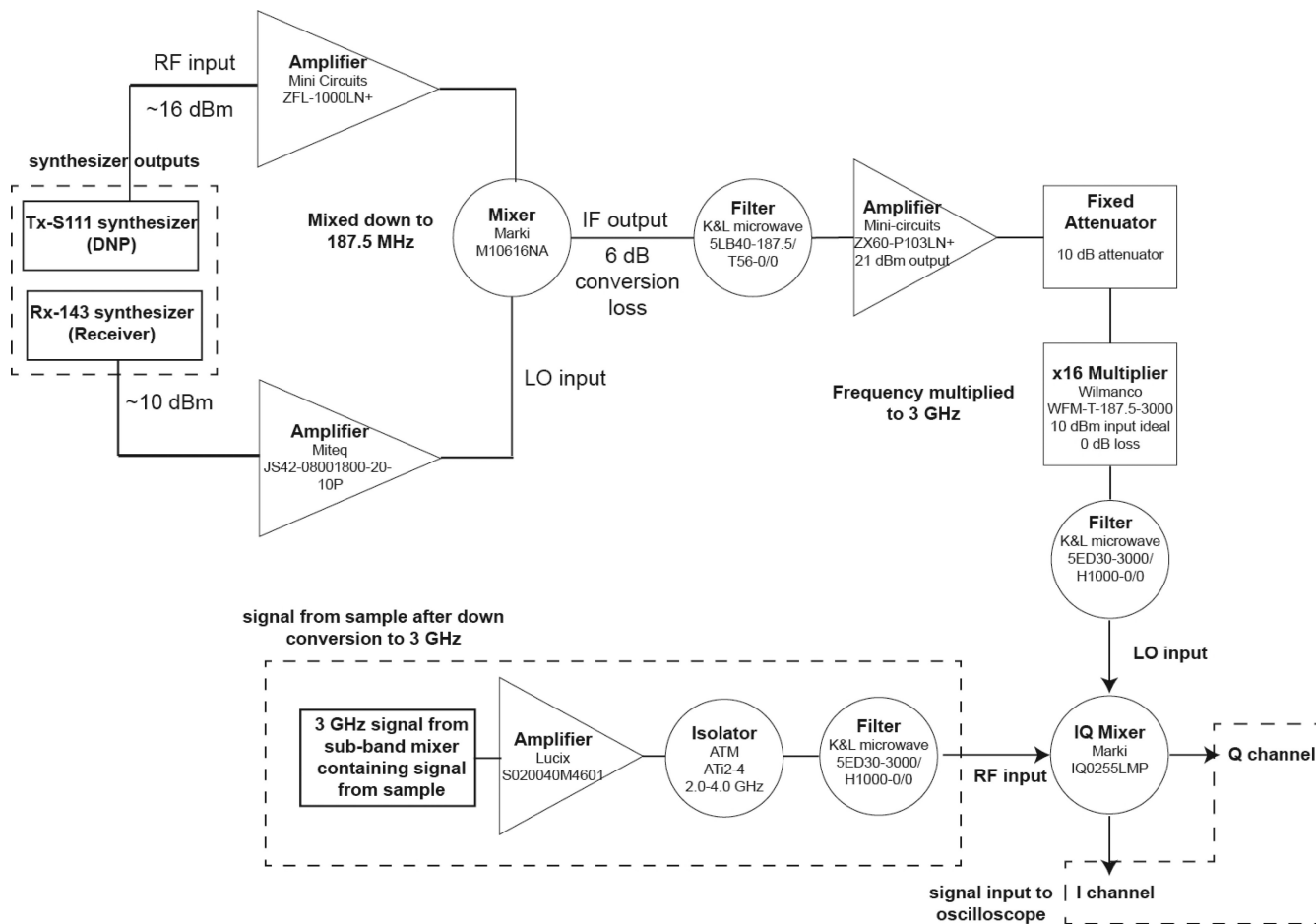
Figure A2 Detailed list of IF stage components for 200 GHz SHDD scheme. The components shown here are used to generate a 3 GHz reference signal that is eventually fed into the LO input of the IQ Mixer. A short description of this electronic circuit is provided in the text above the figure.

10.3. MW components used in homebuilt part of pulse forming unit

Component	Company	Part Number
SP2T Switch	**General Microwave**	**F9120AH**
Voltage Control Phase Shifter	**Spacek Labs**	**SLSP-122–25V**
Isolator	**Quest**	**SR0812T13**
Combiner	**Mini-Circuits**	**ZX10-2-126-S+**
Manual Control Phase Shifter	**Aeroflex**	**980-4**
20 dBm Amp	**Mini-Circuits**	**ZX60-183-S+**

10.4. Quasi optical analysis of the Martin-Puplett Interferometer circuit

QO analysis of the Martin-Puplett interferometer circuit was performed in order to help identify the source of the high MW power loss that resulted in poor DNP performance observed for this QO circuit. Paraxial analysis based on the 3D model of the QO circuit in SolidWorks and beam waist calculations for the fundamental Gaussian free space mode [116] demonstrated absence of significant vignetting of the 99% encircled energy beam for all of the components. The physical optics option of ZEMAX® EE, a commercial optical design software, was used for more detailed analysis of the setup. System efficiency was determined at 99.8% (1.2% energy losses) up to the waveguide, where system efficiency is defined as the transmission energy through the circuit. The coupling coefficient for ideal optics positions was determined by the overlap integral between the incoming MW wavefront and the waveguide fundamental mode to be 88.6%. The coupling coefficient has a maximum value of 1, where some of the causes for reductions in the coupling coefficient are vignetting, absorption, and mismatching of the MW beam and waveguide amplitude and/or phase. The total power coupling coefficient is the product of the system efficiency and the coupling coefficient, which yielded 88.4 %. Additionally, the transition between HE_{11} and Gaussian modes typically has a 2% conversion loss [105,117], resulting in a total ideal coupling efficiency between the source and waveguide of 86.4% for an idealized Martin-Puplett interferometer circuit. The equations used to calculate the total power coupling efficiency can be found in the ZEMAX EE e-manual under the subsection of single mode coupling. One possible source of misalignment was identified as a tilt of the moving roof mirror in the interferometer. The wavefront caused by the tilted roof mirror will have distorted phases, decreasing the coupling coefficient to the HE_{11} mode of the waveguide. In addition, higher order modes will be excited by the tilted wavefront, according to the following equation:

$$\frac{P(\Delta\theta)}{P_0} = 4.2 \cdot \left(\frac{a \cdot \Delta\theta}{\lambda_0}\right)^2$$

where θ is the wavefront tilt in radians, a is the radius of the waveguide, and λ_0 is the wavelength of the MW beam [107]. For a 200 GHz beam coupled to our 12.5 mm waveguide, a tilt of the wavefront by 1° (0.5° tilt of the roof mirror) will cause 2.2 % of the MW beam to be coupled to higher order modes. For this same 1° vertical tilt of the wavefront, the calculated system loss was 57.2% (due to the energy vignetting at the waveguide), and the coupling integral was 61.3%, resulting in a total system efficiency of 36.1% - more than 50% less compared to the ideal optics arrangement. Additional loss in DNP efficiency would result from the interference fringes produced by the two tilted wavefronts after the interferometer (not calculated in ZEMAX). Observations with the array detector, Pyrocam III, at the position of the waveguide confirmed the presence of two wavefronts with the use of an additional polarizer that helped to isolate the divergent wavefronts. This indicated that the movable roof mirror was indeed tilted and the cause of poor DNP performance. Upon adjustment of the roof mirror tilt, an improved Gaussian shape of the beam and a significant increase of MW power was observed as predicted by the simulations.

References

1. Rossini AJ, Zagdoun A, Lelli M, Gajan D, Rascón F, Rosay M, et al. One hundred fold overall sensitivity enhancements for Silicon-29 NMR spectroscopy of surfaces by dynamic nuclear polarization with CPMG acquisition. Chem. Sci. 2012; 3:108–115.

2. Guo Z, Kobayashi T, Wang L-L, Goh TW, Xiao C, a Caporini M, et al. Selective Host-Guest Interaction between Metal Ions and Metal-Organic Frameworks Using Dynamic Nuclear Polarization Enhanced Solid-State NMR Spectroscopy. Chem. - A Eur. J. 2014; 20:16308–16313.

3. Lund A, Hsieh M-F, Siaw T-A, Han S-I. Direct dynamic nuclear polarization targeting catalytically active 27 Al sites. Phys. Chem. Chem. Phys. 2015; 17:25449–25454. [PubMed: 26365719]

4. Blanc F, Sperrin L, Jefferson Da, Pawsey S, Rosay M, Grey CP. Dynamic Nuclear Polarization Enhanced Natural Abundance 17 O Spectroscopy. J. Am. Chem. Soc. 2013; 135:2975–2978. [PubMed: 23379257]

5. Lafon O, Thankamony ASL, Rosay M, Aussenac F, Lu X, Trébosc J, et al. Indirect and direct 29 Si dynamic nuclear polarization of dispersed nanoparticles. Chem. Commun. 2013; 49:2864–2866.

6. Pourpoint F, Thankamony ASL, Volkringer C, Loiseau T, Trébosc J, Aussenac F, et al. Probing 27 Al- 13 C proximities in metal-organic frameworks using dynamic nuclear polarization enhanced NMR spectroscopy. Chem. Commun. 2014; 50:933–935.

7. Vitzthum V, Miéville P, Carnevale D, a Caporini M, Gajan D, Copéret C, et al. Dynamic nuclear polarization of quadrupolar nuclei using cross polarization from protons: surface-enhanced aluminium-27 NMR. Chem. Commun. 2012; 48:1988.

8. Rossini AJ, Zagdoun A, Lelli M, Lesage A, Copéret C, Emsley L. Dynamic Nuclear Polarization Surface Enhanced NMR Spectroscopy. Acc. Chem. Res. 2013; 46:1942–1951. [PubMed: 23517009]

9. Lee D, Duong NT, Lafon O, De Paëpe G. Primostrato Solid-State NMR Enhanced by Dynamic Nuclear Polarization: Pentacoordinated Al 3+ Ions Are Only Located at the Surface of Hydrated γ-Alumina. J. Phys. Chem. C. 2014; 118:25065–25076.

10. Perras FA, Kobayashi T, Pruski M. Natural Abundance 17 O DNP Two-Dimensional and Surface-Enhanced NMR Spectroscopy. J. Am. Chem. Soc. 2015; 137:8336–8339. [PubMed: 26098846]

11. Griffin RG. Spectroscopy: Clear signals from surfaces. Nature. 2010; 468:381–382. [PubMed: 21085166]

12. Lesage A, Lelli M, Gajan D, Caporini Ma, Vitzthum V, Miéville P, et al. Surface enhanced NMR spectroscopy by dynamic nuclear polarization. J. Am. Chem. Soc. 2010; 132:15459–15461. [PubMed: 20831165]

13. Wenk P, Kaushik M, Richter D, Vogel M, Suess B, Corzilius B. Dynamic nuclear polarization of nucleic acid with endogenously bound manganese. J. Biomol. NMR. 2015; 63:97–109. [PubMed: 26219517]

14. Potapov A, Yau W-M, Ghirlando R, Thurber KR, Tycko R. Successive Stages of Amyloid-β Self-Assembly Characterized by Solid-State Nuclear Magnetic Resonance with Dynamic Nuclear Polarization. J. Am. Chem. Soc. 2015; 137:8294–8307. [PubMed: 26068174]

15. Yau W-M, Thurber KR, Tycko R. Synthesis and evaluation of nitroxide-based oligoradicals for low-temperature dynamic nuclear polarization in solid state NMR. J. Magn. Reson. 2014; 244:98–106. [PubMed: 24887201]

16. Ni QZ, Daviso E, V Can T, Markhasin E, Jawla SK, Swager TM, et al. High Frequency Dynamic Nuclear Polarization. Acc. Chem. Res. 2013; 46:1933–1941. [PubMed: 23597038]

17. Renault M, Pawsey S, Bos MP, Koers EJ, Nand D, Tommassen-van Boxtel R, et al. Solid-State NMR Spectroscopy on Cellular Preparations Enhanced by Dynamic Nuclear Polarization. Angew. Chemie Int. Ed. 2012; 51:2998–3001.

18. Potapov A, Thurber KR, Yau W-M, Tycko R. Dynamic nuclear polarization-enhanced 1H-13C double resonance NMR in static samples below 20 K. J. Magn. Reson. 2012; 221:32–40. doi:http://dx.doi.org/10.1016/j.jmr.2012.05.008. [PubMed: 22743540]

19. Pike KJ, Kemp TF, Takahashi H, Day R, Howes AP, V Kryukov E, et al. A spectrometer designed for 6.7 and 14.1T DNP-enhanced solid-state MAS NMR using quasi-optical microwave transmission. J. Magn. Reson. 2012; 215:1–9. [PubMed: 22218011]

20. Jacso T, Franks WT, Rose H, Fink U, Broecker J, Keller S, et al. Characterization of Membrane Proteins in Isolated Native Cellular Membranes by Dynamic Nuclear Polarization Solid-State NMR Spectroscopy without Purification and Reconstitution. Angew. Chemie Int. Ed. 2012; 51:432–435.

21. Salnikov E, Ouari O, Koers E, Sarrouj H, Franks T, Rosay M, et al. Developing DNP/Solid-State NMR Spectroscopy of Oriented Membranes. Appl. Magn. Reson. 2012; 43:91–106.

22. Sergeyev IV, Day La, Goldbourt A, McDermott AE. Chemical Shifts for the Unusual DNA Structure in Pf1 Bacteriophage from Dynamic-Nuclear- Polarization-Enhanced Solid-State NMR Spectroscopy. J. Am. Chem. Soc. 2011; 133:20208–20217. [PubMed: 21854063]

23. Bayro MJ, Debelouchina GT, Eddy MT, Birkett NR, MacPhee CE, Rosay M, et al. Intermolecular structure determination of amyloid fibrils with magic-angle spinning and dynamic nuclear polarization NMR. J. Am. Chem. Soc. 2011; 133:13967–74. [PubMed: 21774549]

24. Barnes AB, De Paëpe G, van der Wel PCA, Hu KN, Joo CG, Bajaj VS, et al. High-Field Dynamic Nuclear Polarization for Solid and Solution Biological NMR. Appl. Magn. Reson. 2008; 34:237–263. http://dx.doi.org/10.1007/s00723-008-0129-1. [PubMed: 19194532]

25. Hall DA. Polarization-Enhanced NMR Spectroscopy of Biomolecules in Frozen Solution. Science (80–.). 1997; 276:930–932.

26. Redfield AG. Nuclear Magnetic Resonance Saturation and Rotary Saturation in Solids. Phys. Rev. 1955; 98:1787. http://link.aps.org/abstract/PR/v98/p1787.

27. Provotorov B. Magnetic resonance saturation in crystals. Zh. Exsp. Teor. Fiz. 1962; 14:1126–1131.

28. Solomon, I. Magnetic and Electric Resonance and Relaxation. In: Smidt, J., editor. Magn. Electr. Reson. Relax. Amsterdam: North-Holland; 1963. p. 25

29. Goldman, M. Spin temperature and nuclear magnetic resonance in solids. Oxford: Clarendon Press; 1970.

30. Abragam A, Goldman M. Principles of dynamic nuclear polarisation. Reports Prog. Phys. 1978; 41:395–467.

31. Atsarkin VA, Kessenikh AV. Dynamic Nuclear Polarization in Solids: The Birth and Development of the Many-Particle Concept. Appl. Magn. Reson. 2012; 43:7–19.

32. Farrar CT, Hall DA, Gerfen GJ, Inati SJ, Griffin RG. Mechanism of dynamic nuclear polarization in high magnetic fields. J. Chem. Phys. 2001; 114:4922–4933. http://link.aip.org/link/?JCP/114/4922/1.

33. Serra SC, Rosso A, Tedoldi F. Electron and nuclear spin dynamics in the thermal mixing model of dynamic nuclear polarization. Phys. Chem. Chem. Phys. 2012; 14:13299. [PubMed: 22918556]

34. Serra SC, Rosso A, Tedoldi F. On the role of electron-nucleus contact and microwave saturation in thermal mixing DNP. Phys. Chem. Chem. Phys. 2013; 15:8416–8428. [PubMed: 23628890]

35. Colombo Serra S, Filibian M, Carretta P, Rosso A, Tedoldi F. Relevance of electron spin dissipative processes to dynamic nuclear polarization via thermal mixing. Phys. Chem. Chem. Phys. 2014; 16:753–764. [PubMed: 24270353]

36. Jannin S, Comment A, Kurdzesau F, Konter JA, Hautle P, van den Brandt B, et al. A 140 GHz prepolarizer for dissolution dynamic nuclear polarization. J. Chem. Phys. 2008; 128:241102. [PubMed: 18601309]

37. De Luca A, Rosso A. Dynamic Nuclear Polarization and the Paradox of Quantum Thermalization. Phys. Rev. Lett. 2015; 115:080401. [PubMed: 26340169]

38. Hovav Y, Feintuch A, Vega S. Theoretical aspects of dynamic nuclear polarization in the solid state: The solid effect. J. Magn. Reson. 2010; 207:176–189. doi:http://dx.doi.org/10.1016/j.jmr.2010.10.016. [PubMed: 21084205]

39. Hovav Y, Feintuch A, Vega S. Dynamic nuclear polarization assisted spin diffusion for the solid effect case. J. Chem. Phys. 2011; 134:74509–74520. http://dx.doi.org/10.1063/1.3526486.

40. Hovav Y, Levinkron O, Feintuch A, Vega S. Theoretical Aspects of Dynamic Nuclear Polarization in the Solid State: The Influence of High Radical Concentrations on the Solid Effect and Cross Effect Mechanisms. Appl. Magn. Reson. 2012; 43:21–41.

41. Hovav Y, Feintuch A, Vega S. Theoretical aspects of dynamic nuclear polarization in the solid state - The cross effect. J. Magn. Reson. 2012; 214:29–41. doi:http://dx.doi.org/10.1016/j.jmr.2011.09.047. [PubMed: 22119645]

42. Hovav Y, Feintuch A, Vega S. Theoretical aspects of dynamic nuclear polarization in the solid state - spin temperature and thermal mixing. Phys. Chem. Chem. Phys. 2013; 15:188–203. [PubMed: 23160533]

43. Thurber KR, Tycko R. On mechanisms of dynamic nuclear polarization in solids. Isr. J. Chem. 2014; 0520:39–46.

44. Thurber KR, Tycko R. Perturbation of nuclear spin polarizations in solid state NMR of nitroxide-doped samples by magic-angle spinning without microwaves. J. Chem. Phys. 2014; 140:184201. [PubMed: 24832263]

45. Thurber KR, Tycko R. Theory for cross effect dynamic nuclear polarization under magic-angle spinning in solid state nuclear magnetic resonance: The importance of level crossings. J. Chem. Phys. 2012; 137:84508–84514.

46. Karabanov A, Kwiatkowski G, Köckenberger W. Quantum Mechanical Simulation of Cross Effect DNP Using Krylov-Bogolyubov Averaging. Appl. Magn. Reson. 2012; 43:43–58.

47. Karabanov A, van der Drift A, Edwards LJ, Kuprov I, Köckenberger W. Quantum mechanical simulation of solid effect dynamic nuclear polarisation using Krylov-Bogolyubov time averaging and a restricted state-space. Phys. Chem. Chem. Phys. 2012; 14:2658–2668. [PubMed: 22261996]

48. Karabanov A, Wi niewski D, Lesanovsky I, Köckenberger W. Dynamic Nuclear Polarization as Kinetically Constrained Diffusion. Phys. Rev. Lett. 2015; 115:020404. [PubMed: 26207453]

49. Hovav Y, Shimon D, Kaminker I, Feintuch A, Goldfarb D, Vega S. Effects of the electron polarization on dynamic nuclear polarization in solids. Phys. Chem. Chem. Phys. 2015; 17:6053–6065. [PubMed: 25640165]

50. Siaw TA, Fehr M, Lund A, Latimer A, Walker SA, Edwards DT, et al. Effect of electron spin dynamics on solid-state dynamic nuclear polarization performance. Phys. Chem. Chem. Phys. 2014; 16:18694. [PubMed: 24968276]

51. Shimon D, Feintuch A, Goldfarb D, Vega S. Static (1)H dynamic nuclear polarization with the biradical TOTAPOL: a transition between the solid effect and the cross effect. Phys. Chem. Chem. Phys. 2014; 16:6687–99. [PubMed: 24585094]

52. Shimon D, Hovav Y, Feintuch A, Goldfarb D, Vega S. Dynamic nuclear polarization in the solid state: a transition between the cross effect and the solid effect. Phys. Chem. Chem. Phys. 2012; 14:5729–5743. [PubMed: 22419272]

53. Banerjee D, Shimon D, Feintuch A, Vega S, Goldfarb D. The interplay between the solid effect and the cross effect mechanisms in solid state 13C DNP at 95 GHz using trityl radicals. J. Magn. Reson. 2013; 230:212–219. doi:http://dx.doi.org/10.1016/j.jmr.2013.02.010. [PubMed: 23522876]

54. Hovav Y, Kaminker I, Shimon D, Feintuch A, Goldfarb D, Vega S. The electron depolarization during dynamic nuclear polarization: measurements and simulations -C4CP03825H. Phys. Chem. Chem. Phys. 2014; 17:226–44. [PubMed: 25384575]

55. Hovav Y, Feintuch A, Vega S, Goldfarb D. Dynamic nuclear polarization using frequency modulation at 3.34T. J. Magn. Reson. 2014; 238:94–105. [PubMed: 24333831]

56. Bornet A, Milani J, Vuichoud B, Perez Linde AJ, Bodenhausen G, Jannin S. Microwave frequency modulation to enhance Dissolution Dynamic Nuclear Polarization. Chem. Phys. Lett. 2014; 602:63–67.

57. Kiesewetter MK, Corzilius B, Smith AA, Griffin RG, Swager TM. Dynamic nuclear polarization with a water-soluble rigid biradical. J. Am. Chem. Soc. 2012; 134:4537–40. [PubMed: 22372769]

58. Matsuki Y, Maly T, Ouari O, Karoui H, Le Moigne F, Rizzato E, et al. Dynamic Nuclear Polarization with a Rigid Biradical. Angew. Chemie. 2009; 121:5096–5100.

59. Dane EL, Corzilius B, Rizzato E, Stocker P, Maly T, Smith AA, et al. Rigid orthogonal bis-TEMPO biradicals with improved solubility for dynamic nuclear polarization. J. Org. Chem. 2012; 77:1789–97. [PubMed: 22304384]

60. Zagdoun A, Casano G, Ouari O, Schwarzwälder M, Rossini AJ, Aussenac F, et al. Large Molecular Weight Nitroxide Biradicals Providing Efficient Dynamic Nuclear Polarization at Temperatures up to 200 K. J. Am. Chem. Soc. 2013; 135:12790–12797. [PubMed: 23961876]

61. Thurber KR, Yau W-M, Tycko R. Low-temperature dynamic nuclear polarization at 9.4 T with a 30 mW microwave source. J. Magn. Reson. 2010; 204:303–313. http://www.sciencedirect.com/science/article/pii/S1090780710000868. [PubMed: 20392658]

62. Kubicki DJ, Rossini AJ, Purea A, Zagdoun A, Ouari O, Tordo P, et al. Amplifying dynamic nuclear polarization of frozen solutions by incorporating dielectric particles. J. Am. Chem. Soc. 2014; 136:15711–8. [PubMed: 25285480]

63. Mentink-Vigier F, Akbey Ü, Hovav Y, Vega S, Oschkinat H, Feintuch A. Fast passage dynamic nuclear polarization on rotating solids. J. Magn. Reson. 2012; 224:13–21. [PubMed: 23000976]

64. Mentink-Vigier F, Akbey Ü, Oschkinat H, Vega S, Feintuch A. Theoretical Aspects of Magic Angle Spinning -Dynamic Nuclear Polarization. J. Magn. Reson. 2015; 258:102–120. [PubMed: 26232770]

65. Corzilius B, Andreas LB, Smith AA, Ni QZ, Griffin RG. Paramagnet induced signal quenching in MAS-DNP experiments in frozen homogeneous solutions. J. Magn. Reson. 2014; 240:113–123. [PubMed: 24394190]

66. Hu K-N, Song C, Yu H, Swager TM, Griffin RG. High-frequency dynamic nuclear polarization using biradicals: A multifrequency EPR lineshape analysis. J. Chem. Phys. 2008; 128:52302–52317. http://link.aip.org/link/?JCP/128/052302/1.

67. Bajaj VS, Farrar CT, Hornstein MK, Mastovsky I, Vieregg J, Bryant J, et al. Dynamic nuclear polarization at 9 T using a novel 250 GHz gyrotron microwave source. J. Magn. Reson. 2003; 160:85–90. http://www.sciencedirect.com/science/article/B6WJX-47YY3HX-1/2/fa6c7d4117944b54cce6c6a168e81fc1. [PubMed: 12615147]

68. Bajaj VS, Hornstein MK, Kreischer KE, Sirigiri JR, Woskov PP, Mak-Jurkauskas ML, et al. 250GHz CW gyrotron oscillator for dynamic nuclear polarization in biological solid state NMR. J. Magn. Reson. 2007; 189:251–279. [PubMed: 17942352]

69. Barnes AB, Mak-Jurkauskas ML, Matsuki Y, Bajaj VS, a van der Wel PC, Derocher R, et al. Cryogenic sample exchange NMR probe for magic angle spinning dynamic nuclear polarization. J. Magn. Reson. 2009; 198:261–70. [PubMed: 19356957]

70. Jawla S, Nanni E, Shapiro M, Mastovsky I, Guss W, Temkin R, et al. Design of a 527 GHz gyrotron for DNP-NMR spectroscopy, in: 2011 Int. Conf. Infrared, Millimeter, Terahertz Waves, IEEE. 2011:1–2.

71. Idehara T, Kosuga K, Agusu L, Ogawa I, Takahashi H, Smith ME, et al. Gyrotron FU CW VII for 300 MHz and 600 MHz DNP-NMR Spectroscopy, J. Infrared, Millimeter. Terahertz Waves. 2010; 31:763–774.

72. Barnes AB, Nanni Ea, Herzfeld J, Griffin RG, Temkin RJ. A 250GHz gyrotron with a 3GHz tuning bandwidth for dynamic nuclear polarization. J. Magn. Reson. 2012; 221:147–153. [PubMed: 22743211]

73. Kumar N, Singh U, Sinha AK. Design of 132GHz gyrotron with 3GHz tunability for 200MHz DNP/NMR spectrometer. Infrared Phys. Technol. 2015; 68:44–51.

74. Becerra LRR, Gerfen GJJ, Bellew BFF, Bryant JAA, Hall DAA, Inati SJJ, et al. A Spectrometer for Dynamic Nuclear Polarization and Electron Paramagnetic Resonance at High Frequencies. J. Magn. Reson. Ser. A. 1995; 117:28–40.

75. Becerra L, Gerfen G, Temkin R, Singel D, Griffin R. Dynamic nuclear polarization with a cyclotron resonance maser at 5 T. Phys. Rev. Lett. 1993; 71:3561–3564. [PubMed: 10055008]

76. Matsuki Y, Ueda K, Idehara T, Ikeda R, Ogawa I, Nakamura S, et al. Helium-cooling and -spinning dynamic nuclear polarization for sensitivity-enhanced solid-state NMR at 14T and 30K. J. Magn. Reson. 2012; 225:1–9. [PubMed: 23079589]

77. Bouleau E, Saint-Bonnet P, Mentink-Vigier F, Takahashi H, Jacquot J-F, Bardet M, et al. Pushing NMR sensitivity limits using dynamic nuclear polarization with closed-loop cryogenic helium sample spinning. Chem. Sci. 2015

78. Idehara T, Tatematsu Y, Yamaguchi Y, Khutoryan EM, Kuleshov aN, Ueda K, et al. The Development of 460 GHz gyrotrons for 700 MHz DNP-NMR spectroscopy, J. Infrared, Millimeter. Terahertz Waves. 2015; 36:613–627.

79. Hoff DEM, Albert BJ, Saliba EP, Scott FJ, Choi EJ, Mardini M, et al. Frequency swept microwaves for hyperfine decoupling and time domain dynamic nuclear polarization. Solid State Nucl. Magn. Reson. 2015; 72:79–89. [PubMed: 26482131]

80. Lelli M, Rossini AJ, Casano G, Ouari O, Tordo P, Lesage A, et al. Hydrophobic radicals embedded in neutral surfactants for dynamic nuclear polarization of aqueous environments at 9.4 Tesla. Chem. Commun. (Camb). 2014; 50:10198–201. [PubMed: 24871229]

81. Lelli M, Gajan D, Lesage A, Caporini MA, Vitzthum V, Miéville P, et al. Fast characterization of functionalized silica materials by silicon-29 surface-enhanced NMR spectroscopy using dynamic nuclear polarization. J. Am. Chem. Soc. 2011; 133:2104–7. [PubMed: 21280606]

82. Ardenkjaer-Larsen JH, Fridlund B, Gram A, Hansson G, Hansson L, Lerche MH, et al. Increase in signal-to-noise ratio of > 10,000 times in liquid-state NMR. Proc. Natl. Acad. Sci. U. S. A. 2003; 100:10158–63. [PubMed: 12930897]

83. Leggett J, Hunter R, Granwehr J, Panek R, Perez-Linde AJ, Horsewill AJ, et al. A dedicated spectrometer for dissolution DNP NMR spectroscopy. Phys. Chem. Chem. Phys. 2010; 12:5883. [PubMed: 20458428]

84. Harris T, Degani H, Frydman L. Hyperpolarized 13C NMR studies of glucose metabolism in living breast cancer cell cultures. NMR Biomed. 2013; 26:1831–1843. [PubMed: 24115045]

85. Lee Y, Heo GS, Zeng H, Wooley KL, Hilty C. Detection of Living Anionic Species in Polymerization Reactions Using Hyperpolarized NMR. J. Am. Chem. Soc. 2013; 135:4636–4639. [PubMed: 23461287]

86. Lumata L, Merritt ME, Malloy CR, Sherry AD, Kovacs Z. Impact of Gd3+ on DNP of [1-13C]pyruvate doped with trityl OX063, BDPA, or 4-oxo-TEMPO. J. Phys. Chem. A. 2012; 116:5129–38. [PubMed: 22571288]

87. Jannin S, Bornet A, Melzi R, Bodenhausen G. High field dynamic nuclear polarization at 6.7T: Carbon-13 polarization above 70% within 20min. Chem. Phys. Lett. 2012; 549:99–102.

88. Granwehr J, Leggett J, Köckenberger W. A low-cost implementation of EPR detection in a dissolution DNP setup. J. Magn. Reson. 2007; 187:266–276. [PubMed: 17560151]

89. Smith AA, Corzilius B, Bryant JA, DeRocher R, Woskov PP, Temkin RJ, et al. A 140GHz pulsed EPR/212MHz NMR spectrometer for DNP studies. J. Magn. Reson. 2012; 223:170–179. [PubMed: 22975246]

90. Feintuch A, Shimon D, Hovav Y, Banerjee D, Kaminker I, Lipkin Y, et al. A Dynamic Nuclear Polarization spectrometer at 95GHz/144MHz with EPR and NMR excitation and detection capabilities. J. Magn. Reson. 2011; 209:136–141. http://www.sciencedirect.com/science/article/pii/S1090780710004027. [PubMed: 21296015]

91. Goldfarb D, Lipkin Y, Potapov A, Gorodetsky Y, Epel B, Raitsimring AM, et al. HYSCORE and DEER with an upgraded 95GHz pulse EPR spectrometer. J. Magn. Reson. 2008; 194:8–15. [PubMed: 18571956]

92. Thurber KR, Potapov A, Yau W-M, Tycko R. Solid state nuclear magnetic resonance with magic-angle spinning and dynamic nuclear polarization below 25 K. J. Magn. Reson. 2013; 226:100–106. doi:http://dx.doi.org/10.1016/j.jmr.2012.11.009. [PubMed: 23238592]

93. Armstrong BD, Edwards DT, Wylde RJ, Walker SA, Han S. A 200 GHz dynamic nuclear polarization spectrometer. Phys. Chem. Chem. Phys. 2010; 12:5920–5926. http://dx.doi.org/10.1039/c002290j. [PubMed: 20461268]

94. Smith GM, Lesurf JCG, Mitchell RH, Riedi PC. Quasi-optical cw mm-wave electron spin resonance spectrometer. Rev. Sci. Instrum. 1998; 69:3924.

95. Lynch WB, Earle KA, Freed JH. 1-mm wave ESR spectrometer. Rev. Sci. Instrum. 1988; 59:1345.

96. Earle KA, Tipikin DS, Freed JH. Far-infrared electron-paramagnetic-resonance spectrometer utilizing a quasioptical reflection bridge. Rev. Sci. Instrum. 1996; 67:2502.

97. Takahashi S, Brunel L-C, Edwards DT, van Tol J, Ramian G, Han S, et al. Pulsed electron paramagnetic resonance spectroscopy powered by a free-electron laser. Nature. 2012; 489:409–413. http://dx.doi.org/10.1038/nature11437. [PubMed: 22996555]

98. van Tol J, Brunel L-CC, Wylde RJ. A quasioptical transient electron spin resonance spectrometer operating at 120 and 240 GHz. Rev. Sci. Instrum. 2005; 76:74101.

99. Muller F, Hopkins MA, Coron N, Grynberg M, Brunel LC, Martinez G. A high magnetic field EPR spectrometer. Rev. Sci. Instrum. 1989; 60:3681–3684.

100. Rohrer M, Brügmann O, Kinzer B, Prisner TF. High-field/high-frequency EPR spectrometer operating in pulsed and continuous-wave mode at 180 GHz. Appl. Magn. Reson. 2001; 21:257–274.

101. Epel B, Gromov I, Stoll S, Schweiger A, Goldfarb D. Spectrometer manager: A versatile control software for pulse EPR spectrometers, Concepts Magn. Reson. Part B-Magnetic Reson. Eng. 2005; 26B:36–45.

102. Siaw TA, Walker SA, Armstrong BD, Han S-I. Inductively coupled NMR probe for versatile dynamic nuclear polarization operation at 7 T: observation of $61 \pm 2\%$ ^{1}H polarization at 4 K. J. Magn. Reson. 2012; 221:5–10. [PubMed: 22743536]

103. Walker SA, Edwards DT, Siaw TA, Armstrong BD, Han S. Temperature dependence of high field 13C dynamic nuclear polarization processes with trityl radicals below 35 Kelvin. Phys. Chem. Chem. Phys. 2013; 15:15106. [PubMed: 23925724]

104. Goldsmith PF. Gaussian Beam Mode Expansions for Feed Elements of Various Types. Quasioptical Syst., IEEE Press. 1998:168–170.

105. Abrams R. Coupling losses in hollow waveguide laser resonators. IEEE J. Quantum Electron. 1972; 8:838–843.

106. Doane, JL. Propagation and Mode Coupling in Corrugated and Smooth-Wall Circular Waveguides. In: Button, KJ., editor. Infrared Millim. New York: Waves, Academic Press Inc; 1985. p. 123-170.

107. Thumm MK, Kasparek W. Passive high-power microwave components. IEEE Trans. Plasma Sci. 2002; 30:755–786.

108. Corzilius B, a Smith A, Barnes AB, Luchinat C, Bertini I, Griffin RG. High-field dynamic nuclear polarization with high-spin transition metal ions. J. Am. Chem. Soc. 2011; 133:5648–5651. [PubMed: 21446700]

109. Hyde JS, Strangeway RA, Camenisch TG, Ratke JJ, Froncisz W. W-band frequency-swept EPR. J. Magn. Reson. 2010; 205:93–101. [PubMed: 20462775]

110. van Slageren J, Vongtragool S, Gorshunov B, Mukhin a. a, Karl N, Krzystek J, et al. Frequency-domain magnetic resonance spectroscopy of molecular magnetic materials. Phys. Chem. Chem. Phys. 2003; 5:3837.

111. Takahashi S, Allen DG, Seifter J, Ramian G, Sherwin MS, Brunel L-C, et al. Pulsed EPR spectrometer with injection-locked UCSB free-electron laser. Infrared Phys. Technol. 2008; 51:426–428.

112. Low W. Paramagnetic Resonance Spectrum of Manganese in Cubic MgO and CaF2. Phys. Rev. 1957; 105:793–800.

113. Cho FH, Stepanov V, Takahashi S. A high-frequency electron paramagnetic resonance spectrometer for multi-dimensional, multi-frequency, and multi-phase pulsed measurements. Rev. Sci. Instrum. 2014; 85:075110. [PubMed: 25085176]

114. Morley GW, Brunel L-C, van Tol J. A multifrequency high-field pulsed electron paramagnetic resonance/electron-nuclear double resonance spectrometer. Rev. Sci. Instrum. 2008; 79:064703. [PubMed: 18601425]

115. Edwards DT, Takahashi S, Sherwin MS, Han S. Distance measurements across randomly distributed nitroxide probes from the temperature dependence of the electron spin phase memory time at 240 GHz. J. Magn. Reson. 2012; 223:198–206. [PubMed: 22975249]

116. Self SA. Focusing of spherical Gaussian beams. Appl. Opt. 1983; 22:658. [PubMed: 18195851]

117. Kowalski EJ, Tax DS, Shapiro Ma, Sirigiri JR, Temkin RJ, Bigelow TS, et al. Linearly Polarized Modes of a Corrugated Metallic Waveguide. IEEE Trans. Microw. Theory Tech. 2010; 58:2772–2780.

Highlights

- Modular and versatile design for dual EPR and DNP operation at 7 T.

- Fully customizable quasi optics circuits for MW transmission, detection and diagnostics.

- Automated measurement of DNP frequency profile and power curve.

- DNP enhancement observed up to 90 K and oversaturation observed at 4–6 K

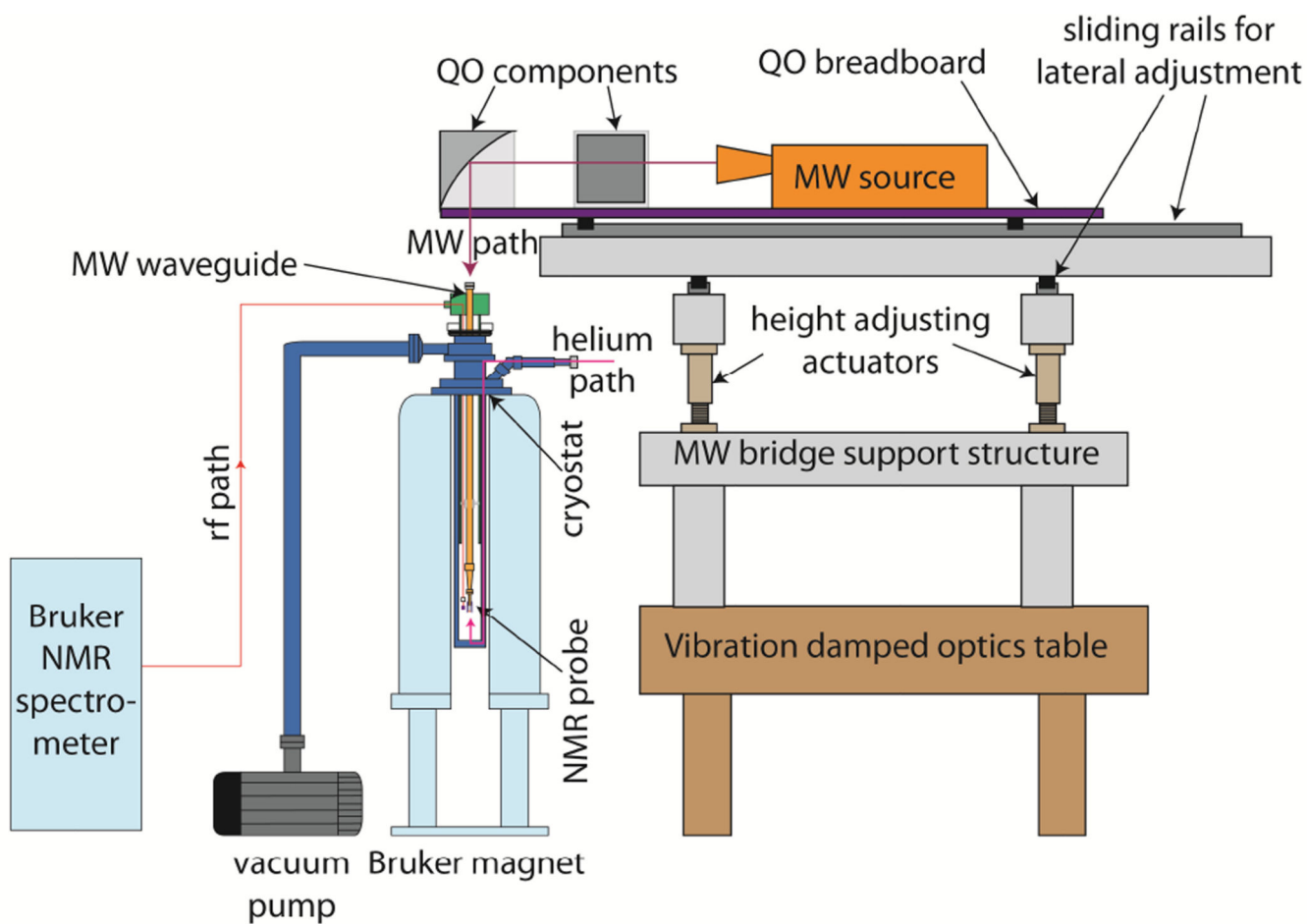- Implementation of frequency stepped CW EPR, pulsed EPR and ELDOR at CW DNP condition.

Figure 1.
Sketch of overall configuration of the UCSB 200 GHz dual EPR/DNP system. Note: EPR detection QO components are located on the MW bridge but not shown (see main text for detailed description).
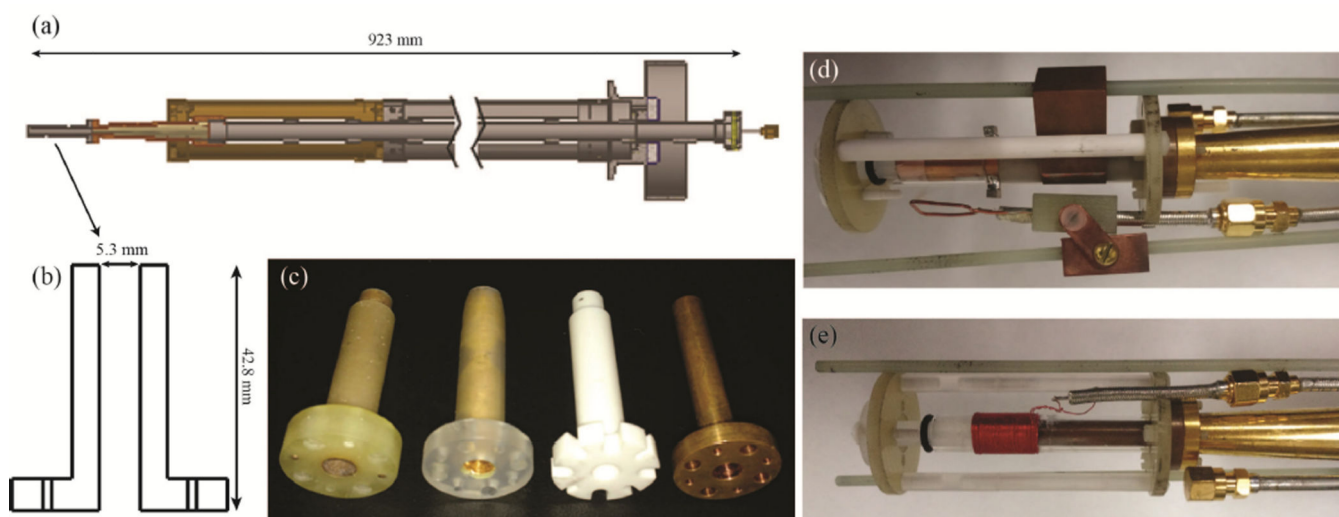
Figure 2.
Details of the probe insert for NMR and EPR detection. (a) Structure of the probe insert with corrugated waveguide, (b) cross sectional sketch showing dimensions of the waveguide extensions (corrugations not shown), (c) the four waveguide extensions listed from left to right: gold with Kel-F support, gold with plastic support, zirconia, and coper, (d) the probe modules with an inductively coupled ^{1}H Alderman-grant coil for DNP/NMR detection, (e) a modulation coil for EPR detection.
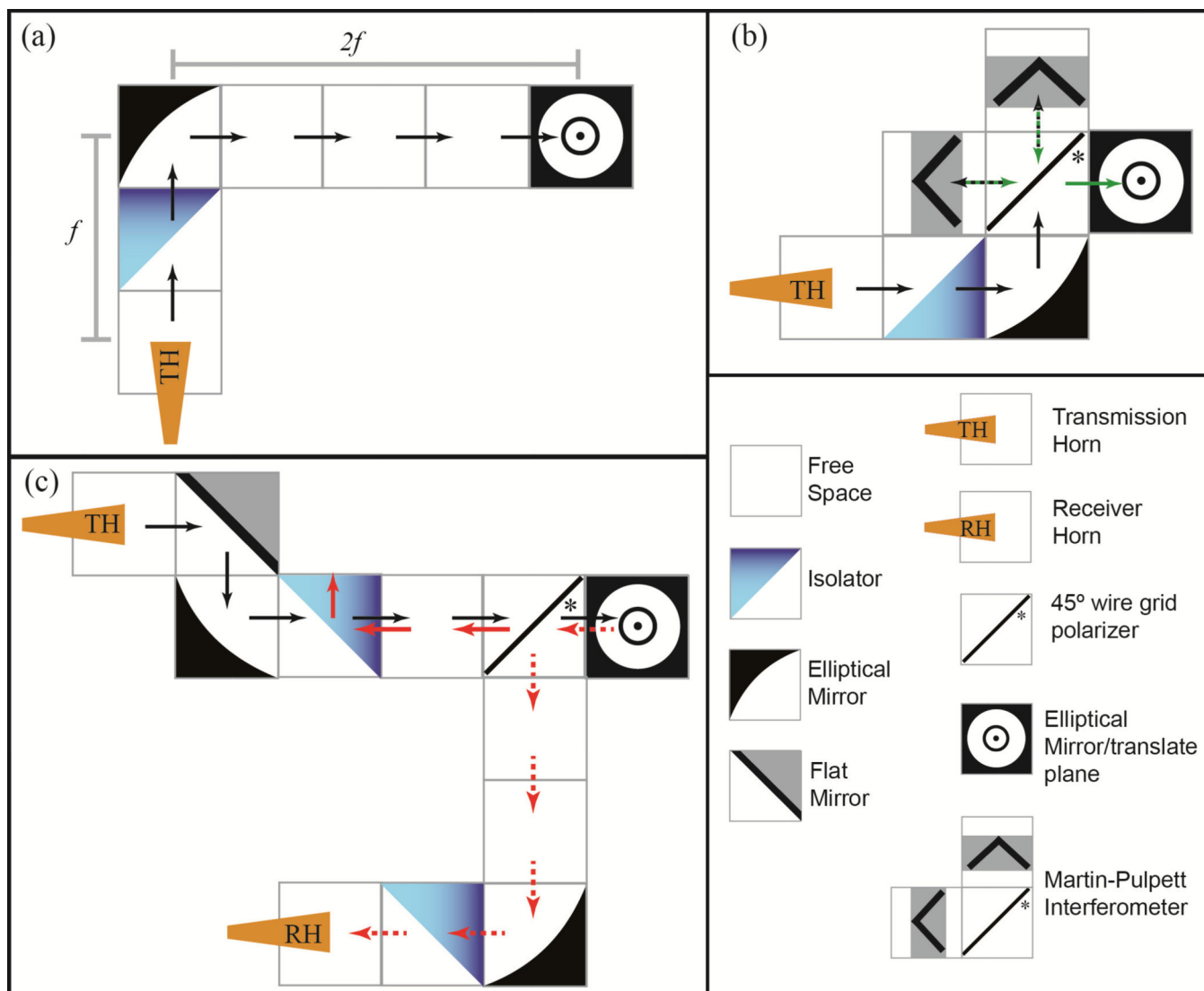
Figure 3.
Schemes of different QO circuits: (a) low-loss DNP circuit (b) Martin-Puplett DNP circuit, (c) dual DNP/EPR circuit. Each tile represents a distance of 12.5 cm ($f/2$). The dark portion of isolator indicates the position of the 45° Faraday rotator. Black arrows represent the incident MW beam; green arrows represent the MW beam after recombining in a Martin-Puplett interferometer; solid red arrows indicate the reflected beam not carrying the EPR signal, which are directed to a MW absorber; dashed red arrows represent the reflected beam carrying the EPR signal that is directed to the receiver horn.
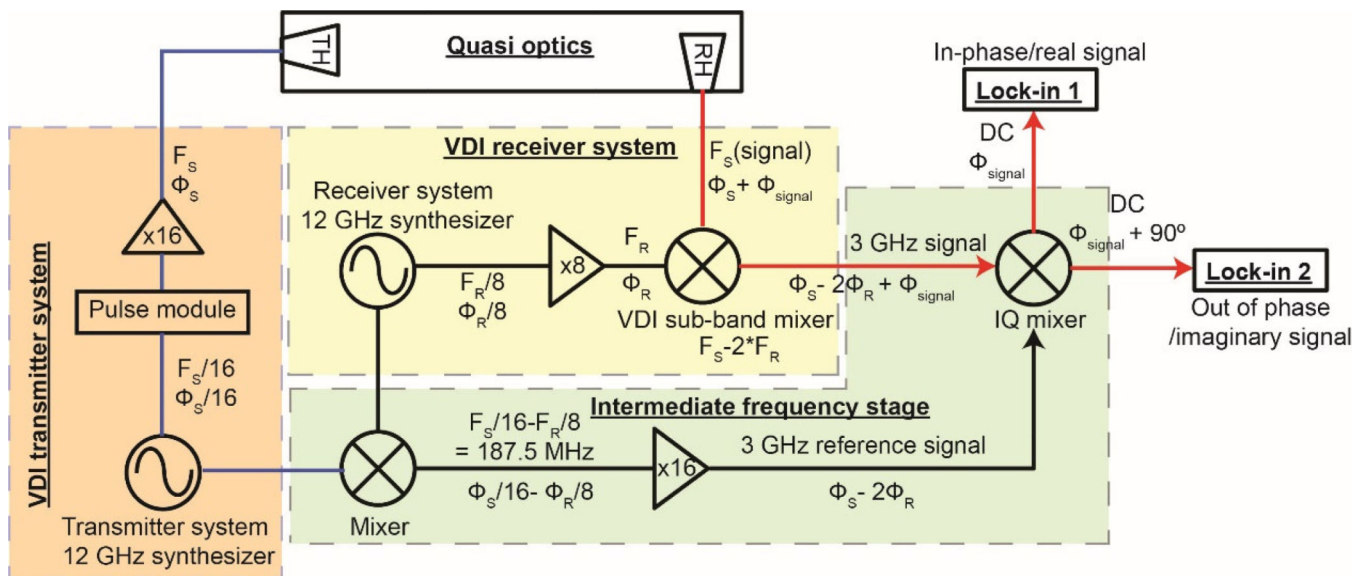
Figure 4.
Schematic representation of the 200 GHz superheterodyne detection system. The yellow block denotes the VDI receiver system; orange block the VDI transmitter system and the green block denotes the IF stage (for full IF stage schematics see Appendix 10.2). Incident transmitted MW beam is denoted as dark blue lines; MW beam carrying EPR signal is shown as red lines. Reference frequencies are shown as black lines.
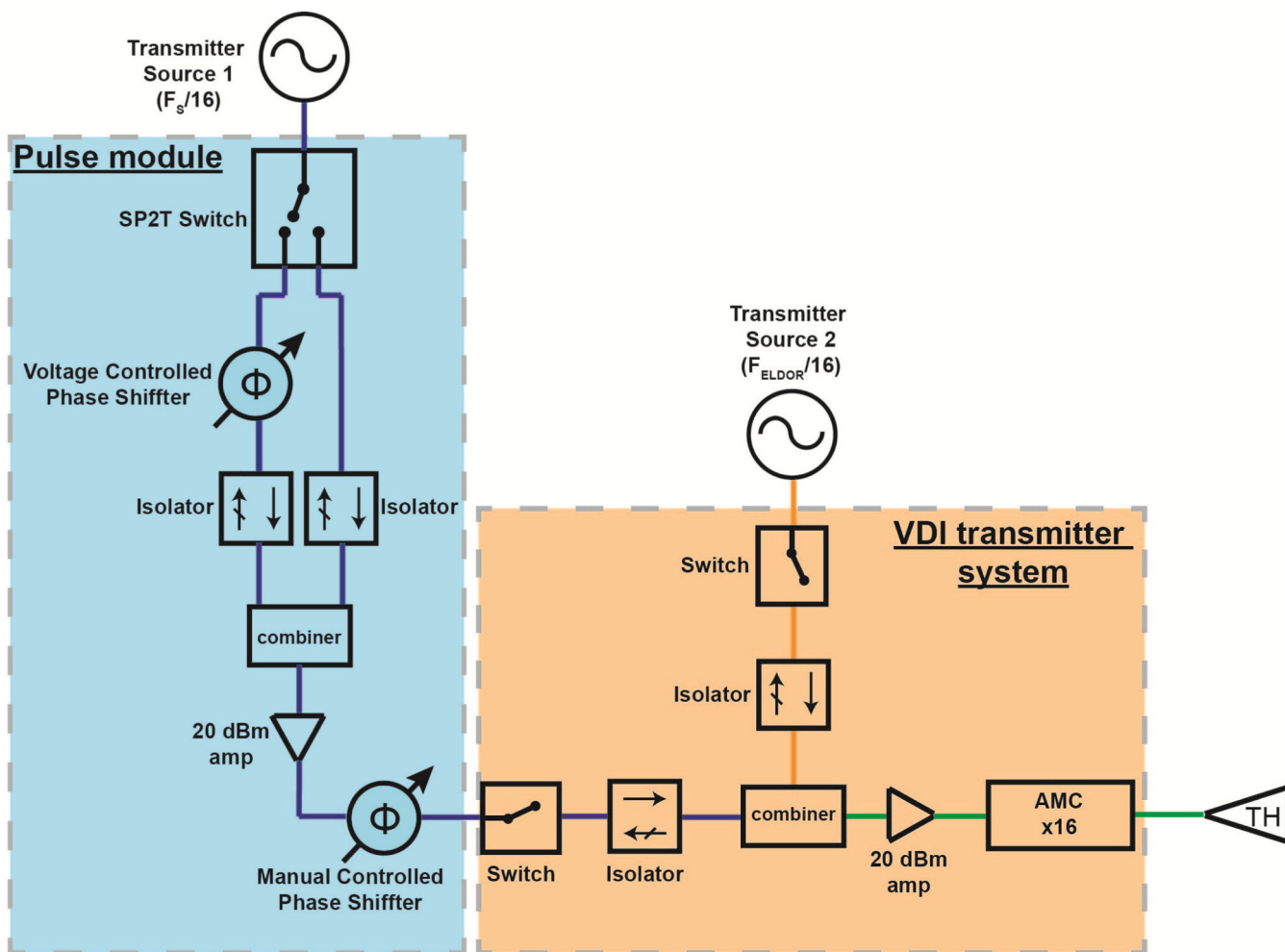
Figure 5.
Schematic representation of the 12 GHz pulse forming unit. Orange block denotes MW components provides as part of the VDI transmitter system; blue block details the components of the homemade pulse forming unit. Blue line denotes the path of ~12 GHz signal at main (F_S) frequency generated by transmitter source 1. Orange line denotes the path ~12 GHz signal at 2nd (F_{ELDOR}) frequency generated by transmitter source 2. Green line denotes the path shared by both F_S and F_{ELDOR} signals. The detailed list of the MW components used in the pulse forming unit is provided in Appendix 10.3.
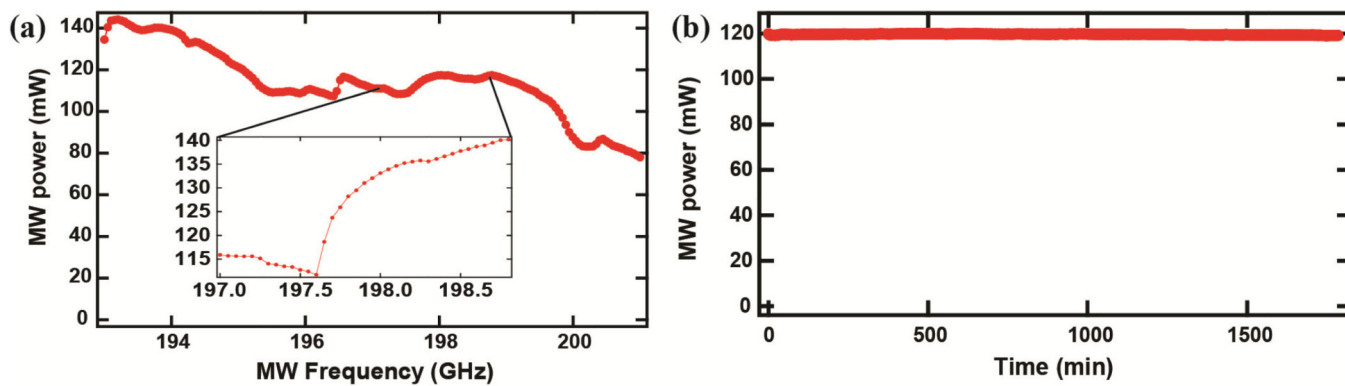
Figure 6.
Power output of MW source a) across the full 8 GHz frequency range. The inset shows the power output across the frequency range used for obtaining DNP spectra of nitroxides between 197. 0 – 198.8 GHz. Lines are to guide the eye. b) Source power stability at 197.7 GHz with no applied attenuation taken over 32 hours of operation. An average power output of 119.6 mW was observed with a variation of power over time < 0.05 %.
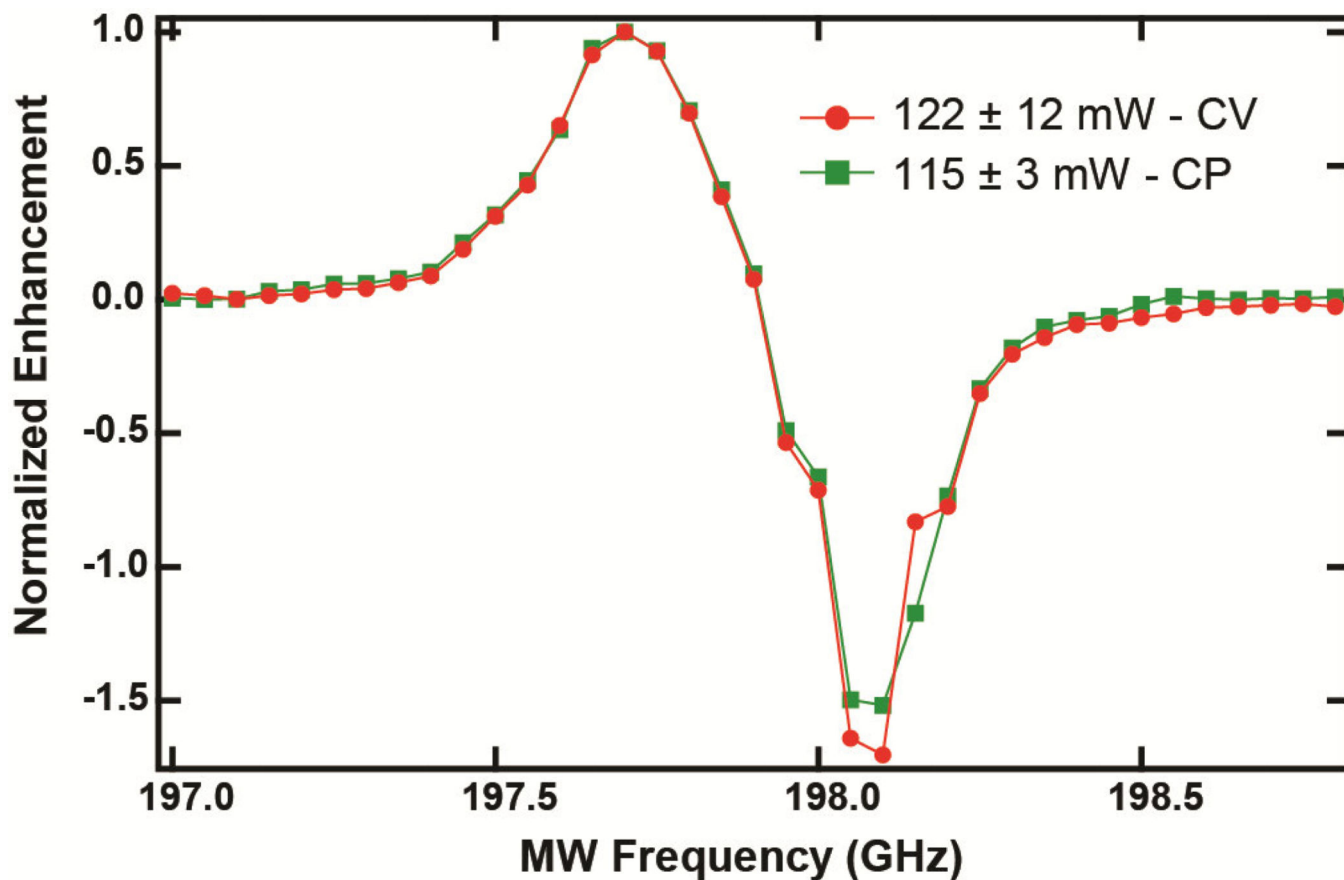
Figure 7.
The DNP spectra of 40 mM 4AT in d_8-glycerol:D_2O:H_2O (50:40:10 v%) measured with two methods: (red circles) no applied attenuation to the AMC of the MW source, denoted as a constant voltage measurement (CV), with an average power of 122 mW over the DNP spectrum range, and (green squares) a frequency dependent attenuation was applied to the AMC of the MW source in order to obtain a constant power output of 115 mW, denoted as a constant power measurement (CP). Lines are to guide the eye.
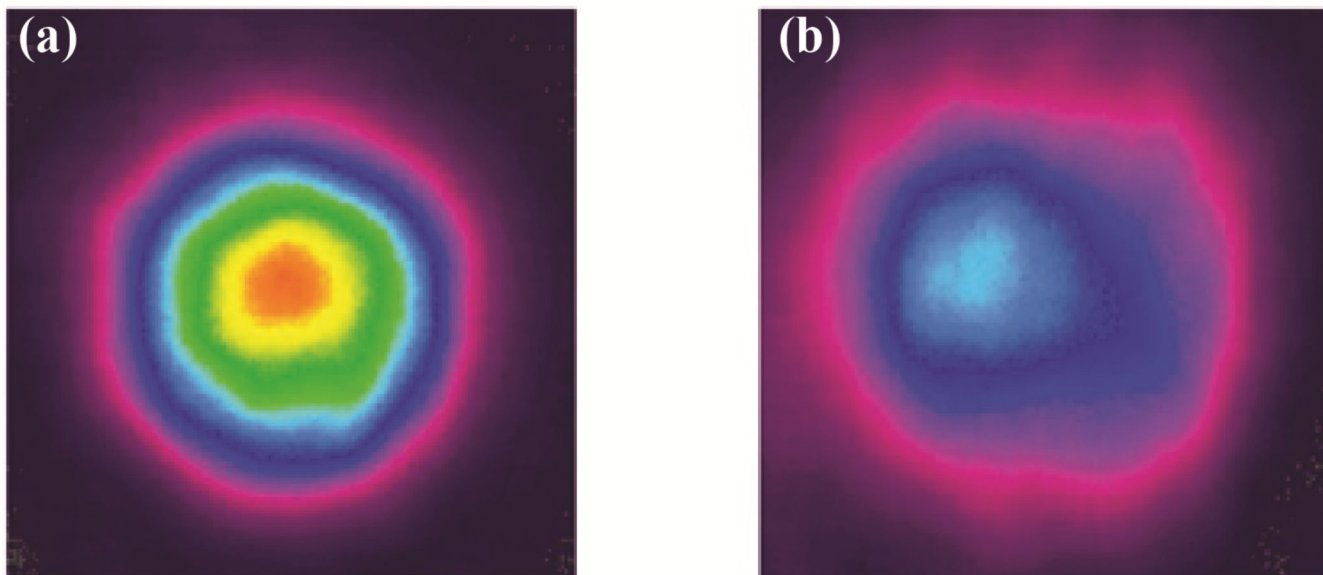
Figure 8.
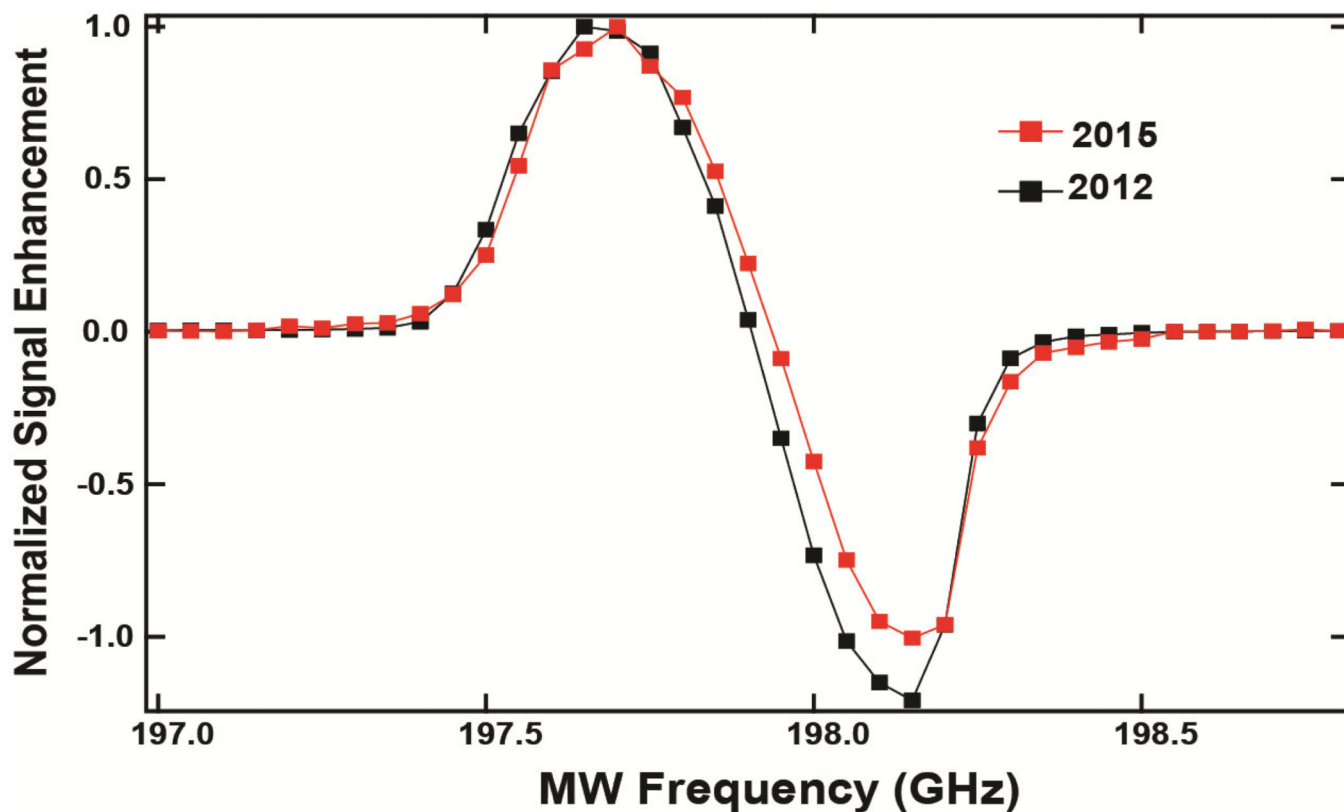Pyrocam images of the MW beam (a) before and (b) after the Martin-Pulpett interferometer.

Figure 9.
Comparison of the DNP spectra of of 40 mM 4-AT in d_8-glycerol:D_2O;H_2O (50:40:10 v%) at 4 K and 7.05 T from 2012 (black square) with the Martin-Pulpett QO circuit and 2015 (red circle) with the low-loss DNP QO circuit. No significant changes were observed. Lines are to guide the eye.
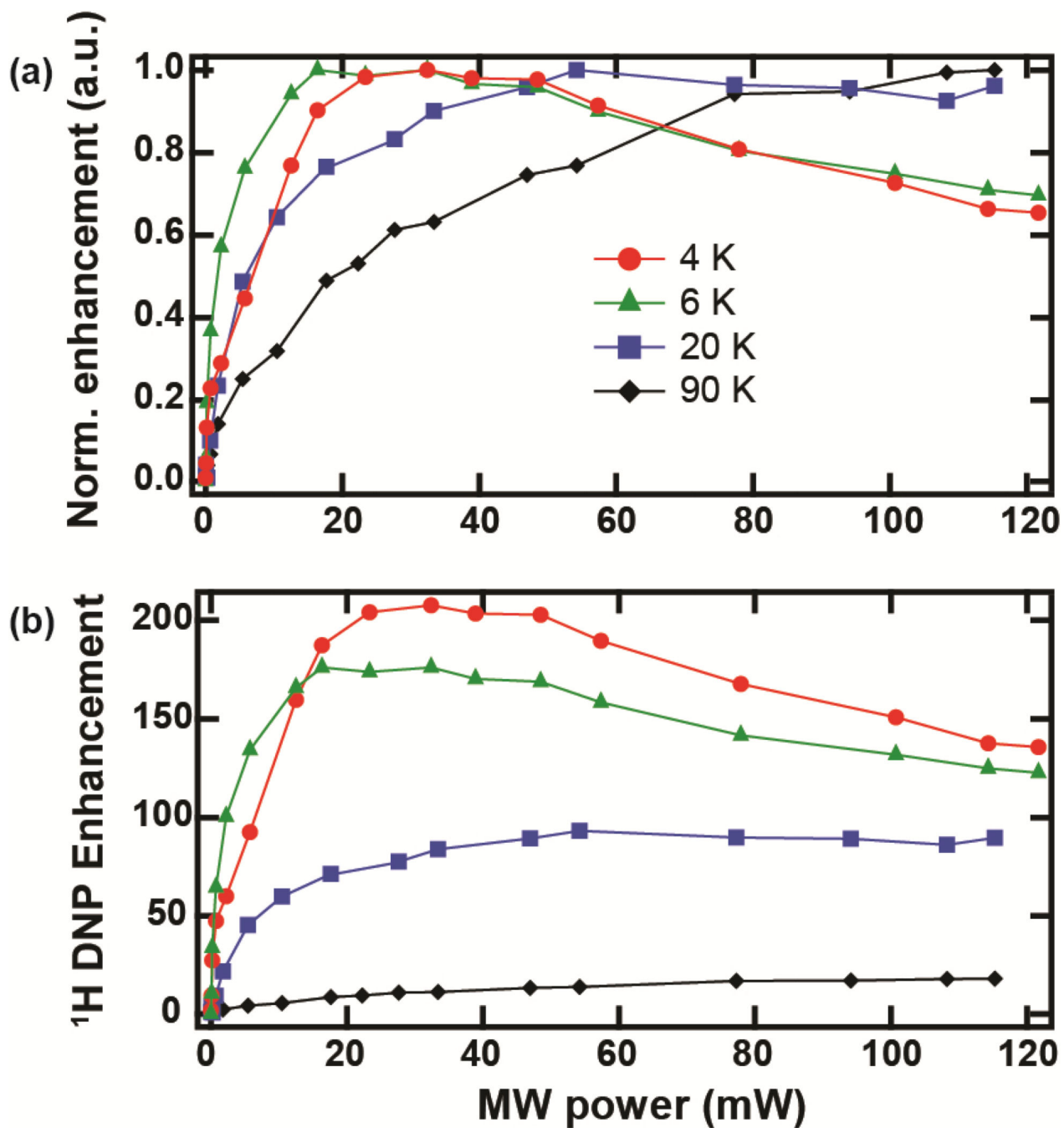
Figure 10.
Temperature dependence of the DNP power curve at 4,6, 20, and 90 K for 40 mM 4-AT in d_8-glycerol:D_2O:H_2O (50:40:10 v%) at 7.05 T. The enhancements values were measured at a MW frequency of 197.7 GHz, plotted as (a) normalized and (b) un-normalized DNP enhancement values, as a function of MW power. Lines are to guide the eye.
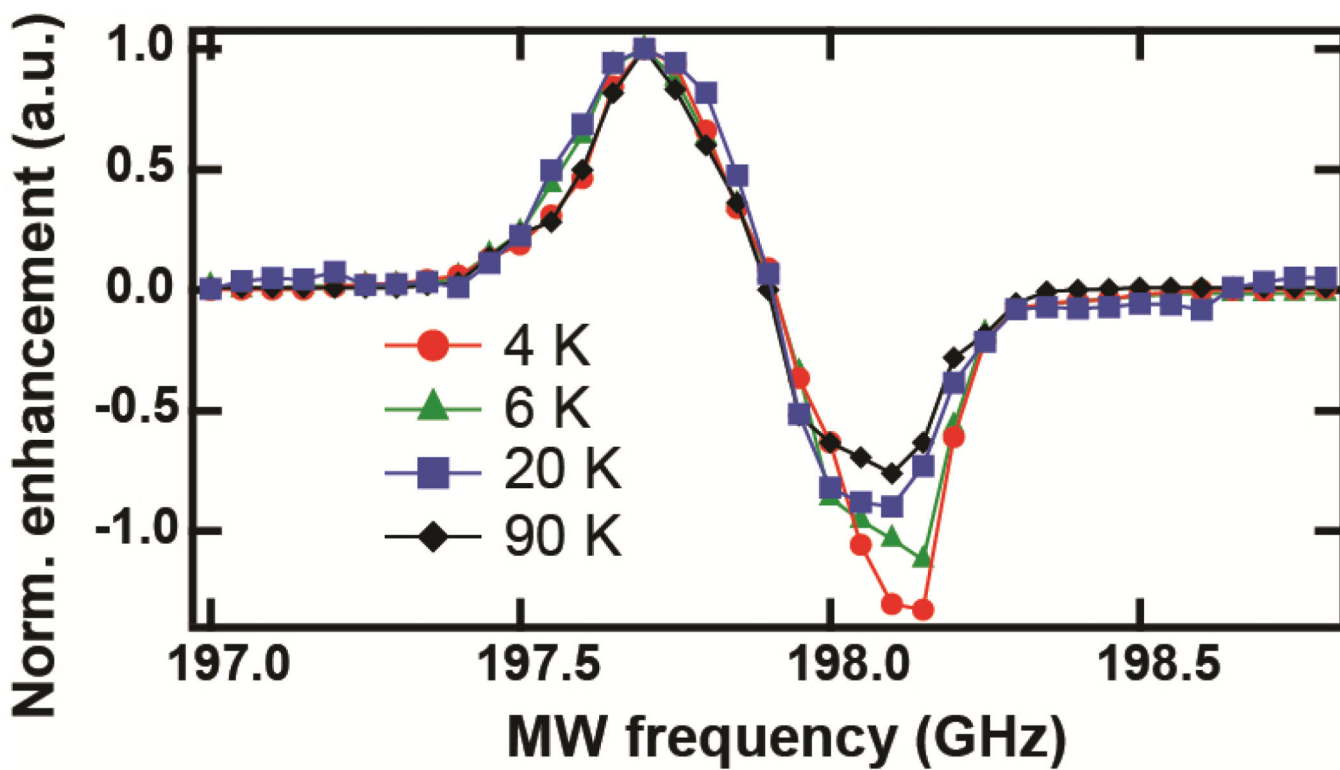
Figure 11.
Temperature dependence of 40 mM 4-AT in d_8-glycerol:D_2O:H_2O (50:40:10 v%) DNP spectra at 4, 6, 20, and 90 K measured with 125 mW of MW output power at 7.05 T. Lines are to guide the eye.
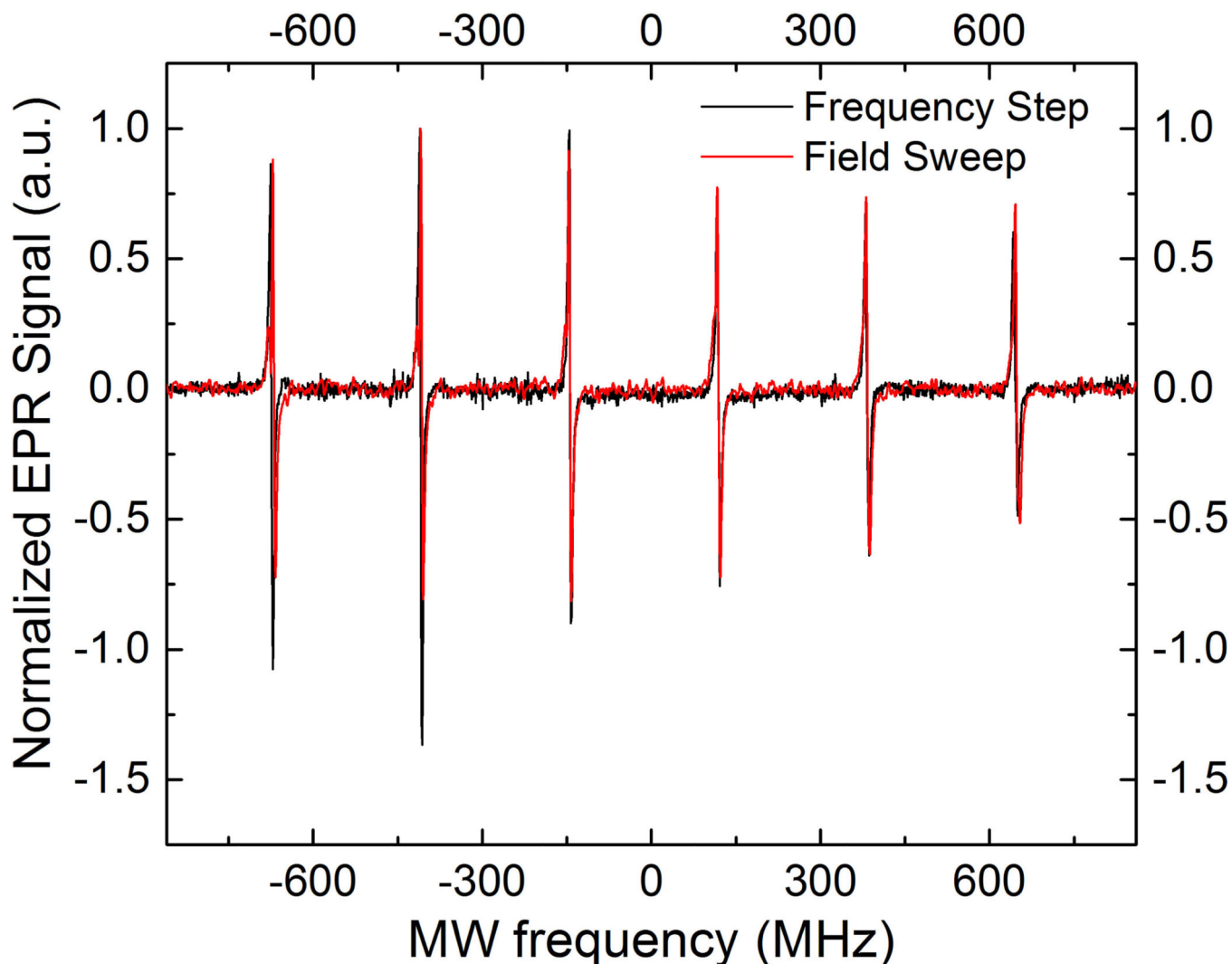
Figure 12.
EPR spectrum of modeling clay containing Mn(II) for frequency swept EPR (black solid line) compared to a field swept spectrum of the same sample taken at 8.5 T (red dashed line). Experimental parameters: frequency sweep spectrum at 7.05 T (~200GHz): mw power when irradiated with 22 ± 1 mW; modulation frequency: 20 kHz, modulation amplitude 0.26 mT, time constant: 30 ms, 10 scans, frequency stepping rate 10 Hz. ZBD detection; field sweep spectrum at 240 GHz: MW power 0.05 mW, field sweep rate: 0.1 mT/s, modulation frequency: 20 kHz, modulation amplitude 0.1 mT, time constant: 200 ms, 1 scan. Phase sensitive detection using SHDD scheme [111].
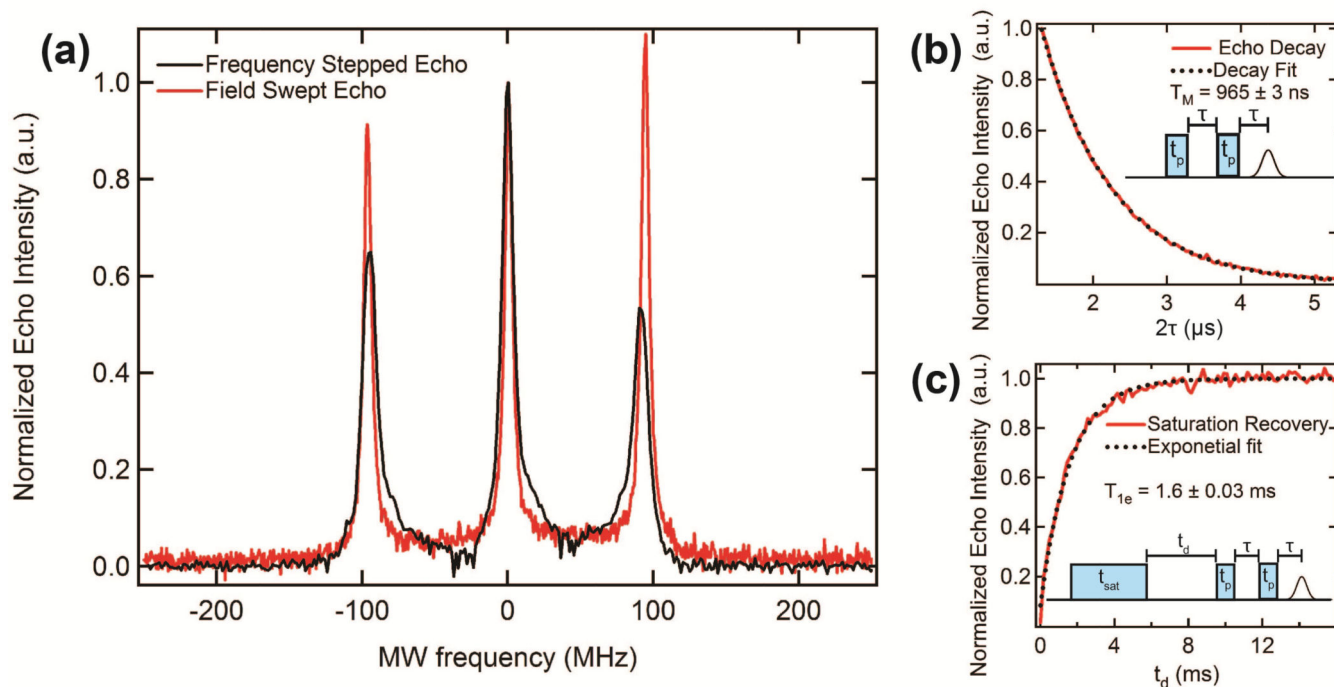
Figure 13.

(a) 200 GHz frequency stepped echo detected spectrum (black) and 240GHz field swept echo detected EPR spectra of P1 centers in diamond. (b) Two pulse echo decay (red) and mono-exponential fit (black). (c) Saturation recovery experiment using the $t_{sat}t_dt_p$-τ-t_p-τ-echo pulse sequence (insert of c) varying the t_{sat} (red) and mono-exponential fit (black). The pulse sequence t_p-τ-t_p-τ-echo (insert of b) was used in (a) and (b); Experimental parameters (a, black): F_S = 197.3 GHz – 197.8 GHz; t_p = 300 ns; τ =500 ns; repetition time 2 ms; no phase cycling. (a, red): magnetic field 8.578 T – 8.589 T; t_p = 500 ns; τ =900 ns; repetition time 10 ms; no phase cycling (b) t_p = 300 ns; varying τ = 500 ns – 2600 ns; repetition time = 2 ms; no phase cycling. (c) t_{sat} = 20 ms; t_p = 300 ns; τ = 900 ns; varying t_d = 1 μs – 16000 μs; repetition time = 40 ms; no phase cycling. For all experiments the magnetic field was set to 7.05 T.
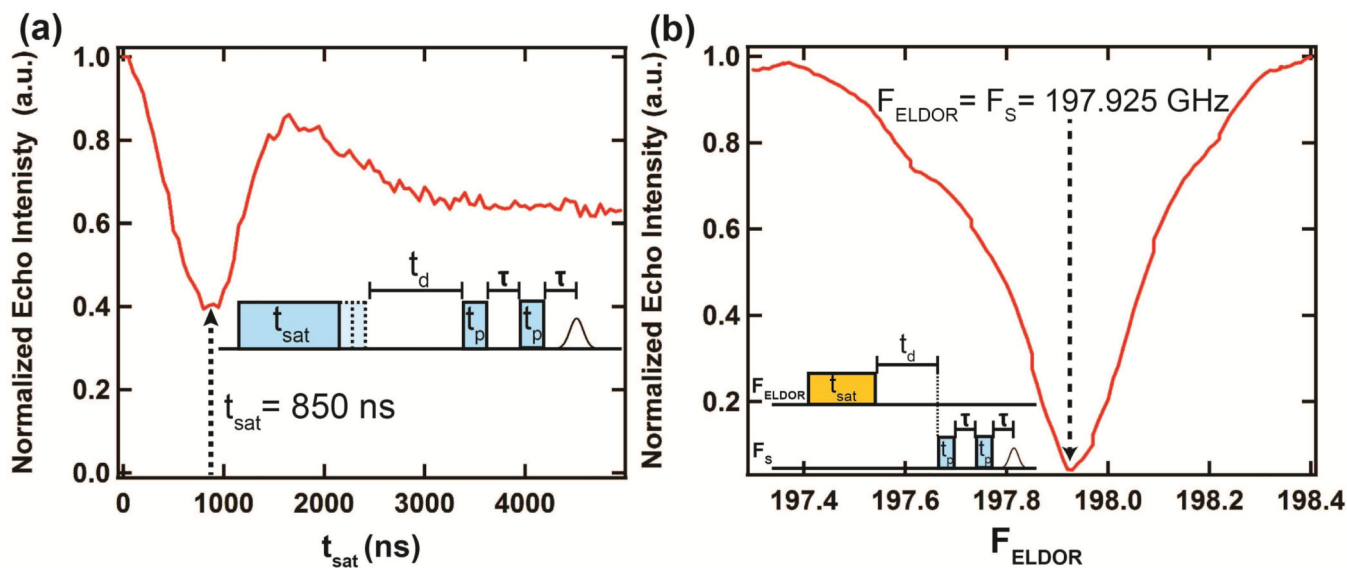
Figure 14.
(a) Echo detected nutation experiment at F_S =197.925 GHz; Experimental parameters: F_S =197.96 GHz; t_p = 500 ns; τ = 500 ns; variable t_{sat} = 0 – 5000 ns; no phase cycling; T = 4K; magnetic field 7.05 T. (b) 200 GHz ELDOR spectra of 40 mM 4AT acquired using the $t_{sat}(F_{ELDOR}) - t_d$ - $t_p(F_S)$-τ-$t_p(F_S)$-τ-echo pulse sequence shown in the insert. Experimental parameters: F_S = 197.925 GHz; F_{ELDOR} = 197.3 – 198.4 GHz; t_{sat} = 50 ms; t_p = 500 ns; τ = 500 ns; two step phase cycle.

Table 1

Summary of the main types of modern ssDNP spectrometers and their current capabilities.

System	Field	Temperature	MW source output	Current system capabilities
Gyrotron-powered DNP	9.4 T 14 T 18.8 T	> 90 K	5–35 W	MAS acquisition, field swept DNP spectra
	9.4 T 14 T	30 K	5–35 W	MAS acquisition, field swept DNP spectra
Dissolution DNP	3.35 T 5 T 6.7 T	1.2 K	90 mW (diode)	Field/Frequency modulation, Frequency swept DNP spectra, MRI metabolic imaging, solution state DNP-enhanced spectroscopy
Nottingham Kockenberger lab dissolution DNP/EPR	3.35 T	1–2 K	180 mW (diode)	Frequency swept DNP spectra, solution state DNP-enhanced spectroscopy, frequency swept CW EPR
	3.35 T	1.5 K	200 mW (diode)	Pulsed and CW EPR, frequency modulation, amplitude modulation, frequency swept DNP spectra, ELDOR, solution state DNP-enhanced spectroscopy
MIT Griffin lab DNP/EPR	5 T	1.4–290 K	120 mW (diode)	Pulsed and field swept echo-EPR, frequency swept DNP spectra, ELDOR, ENDOR, static NMR acquisition
Weizmann Institute Vega and Goldfarb DNP/EPR	3.34 T	2.5–290 K	1 W (diode)	Pulsed and CW EPR, frequency modulation, frequency swept DNP spectra, ELDOR, static NMR acquisition
NIH Tycko lab DNP	9.4 T	20–290 K	0.8 W (EIO) 30 mW (diode)	MAS acquisition, frequency swept DNP (diode source only), field sweep, QO manipulation of MW.
UCSB Han lab DNP/EPR	7 T	4–290 K	140 mW (diode)	Pulsed and CW EPR, frequency swept DNP spectra, static and MAS NMR acquisition, QO manipulation of MW.

Table 2

Comparative loss analysis at 197.7 GHz of individual QO components based off of the quasi optical circuits depicted in Fig. A1(a–e). All QO components were purchased from Thomas Keating Ltd.

Component	Insertion Loss (dB)
isolator	1.3 ± 0.2
Flat mirror[*]	1.9 ± 0.3
waveguide	0.45 ± 0.05
Interferometer	3.3 ± 0.3

[*]
The loss for the flat mirror is position dependent, as explained in the text above.

Table 3

Loss analysis of QO circuits. Theoretical and actual loss of the systems are provided.

QO Design	Theoretical loss (dB)	Actual loss (dB)
Martin-Pulpett	5	7 ± 1
Low-loss DNP	2	2.5 ± 0.3
Dual DNP/EPR	3.7	3.1 ± 0.05

Table 4

Insertion losses for four different types of waveguide extensions, calculated from the pyroelectric readings before and after MW transmission through the waveguide extensions.

Waveguide extension type	Insertion loss from waveguide extension, dB/%	NMR ^{1}H Background Signal
smooth copper waveguide	0/0	No background signal
gold corrugated waveguide with plastic support	0/0	Plastic support causes huge background signal
damaged gold corrugated waveguide with CTFE support	1.46/20	Epoxy resin adds small amount of background signal
zirconia waveguide	7.46/82	No background signal

Table 5

Maximum DNP enhancement, A_{DNP}, and EPR relaxation data values ($T_{1e}T_{SD}W_{flipflop}S_{int}$) for 40 mM 4-AT at 4, 6, 20, and 90 K. The electron spin relaxation data T_{1e} and T_{SD} were acquired at 8.4 T while $W_{flipflop}$ and S_{int} were calculated from T_M measurements published previously [50].

Temperature (K)	DNP (MHz)	Maximum DNP enhancement	T_{1e} (ms)	T_{SD} (ms)	$W_{flipflop}$ (kHz)	S_{int} ($T_{1e}*W_{flipflop}$)
4	450	208	28.9 ± 1.7	4 ± 1	51 ± 54	1477 ± 159
6	450	176	19.5 ± 0.5	3.9 ± 0.3	92 ± 54	1802 ± 156
20	400	94	2.8 ± 0.3	0.5 ± 0.3	155 ± 54	433 ± 59
90	400	18	-	-	-	-